2004

The effects of ion bombardment during deposition upon the properties of hydrogenated amorphous silicon-germanium thin films and photovoltaic devices

Matthew Alan Ring

Iowa State University

The effects of ion bombardment during deposition upon the properties of

hydrogenated amorphous silicon-germanium thin films and photovoltaic devices

by

Matthew Alan Ring

A dissertation submitted to the graduate faculty

in partial fulfillment of the requirements for the degree of

DOCTOR OF PHILOSOPHY

Major: Electrical Engineering

Program of Study Committee:
Vikram Dalal, Major Professor
Alan Constant
Mani Mina
Surya Mallapragada
Gary Tuttle

Iowa State University

Ames, Iowa

2004

UMI Number: 3136345

INFORMATION TO USERS

The quality of this reproduction is dependent upon the quality of the copy submitted. Broken or indistinct print, colored or poor quality illustrations and photographs, print bleed-through, substandard margins, and improper alignment can adversely affect reproduction.

In the unlikely event that the author did not send a complete manuscript and there are missing pages, these will be noted. Also, if unauthorized copyright material had to be removed, a note will indicate the deletion.

UMI®

UMI Microform 3136345

Copyright 2004 by ProQuest Information and Learning Company.

All rights reserved. This microform edition is protected against unauthorized copying under Title 17, United States Code.

Graduate College

Iowa State University

This is to certify that the doctoral dissertation of

Matthew Alan Ring

has met the dissertation requirements of Iowa State University

Signature was redacted for privacy.

Major Professor

Signature was redacted for privacy.

For the Major Program

To Alicia,

without you I could not have completed this dissertation.

Thank you for your support and love

over the past seven years.

iv

TABLE OF CONTENTS

ABSTRACT

Ion bombardment is inherent in the growth of amorphous materials by conventional PECVD methods, such as electron cyclotron resonance (ECR) of radio-frequency (rf) discharge. In these methods plasma ions are necessary to decompose the source gases; however these ions also impinge upon the growing film surface, imparting their energy to the material. In conventional deposition techniques it is difficult to isolate the effects of the ions so a novel approach is taken in this research where an ECR ion source is attached to a "hot-wire" deposition reactor. This unique reaction system allows researchers to vary the ion bombardment density and energy to study the effects of the ion bombardment on the resulting material.

Throughout this research, HW-ECR materials outperformed the HWCVD materials deposited at identical substrate temperatures for photovoltaic applications. The addition of ion bombardment saw a substantial decrease in Urbach energy, hydrogen microstructure, and a corresponding increase in photoconductivity and photosensitivity, regardless of band-gap. During the experiments, the ECR microwave power applied to the reactor was adjusted and showed that as band-gap decreased; less ion energy was required to show improvements in material quality. In addition, a lower filament temperature was required as band gap decreased to maintain a high photoconductivity.

The first ever solar cell devices having intrinsic layers deposited by HW-ECR were deposited in this work, and show that this deposition method can produce solar cells with performance on par with current PECVD and HWCVD materials. In addition, these devices are deposited at much higher growth rates, reducing fabrication time dramatically.

The standard growth model fails to address the role of ion bombardment; however J. Robertson of Cambridge University has proposed a model for hydrogen ions' role in the removal of excess hydrogen. The results presented here support that model, and in addition neutral ions, such as helium, are shown to improve the material. Helium ions are postulated to aide mostly in the surface diffusion of reactive radicals during deposition, as helium is a non-reactive chemical species.

CHAPTER 1: INTRODUCTION

1.1: Background

Researchers have long sought high growth rate processes to produce high quality amorphous materials to facilitate the production of devices containing thick layers of these materials. Hot wire chemical vapor deposition (HWCVD) has recently been the subject of intense research due to the very high growth rates that have been reported in literature using this method. HWCVD is also of interest due to its simplicity and the wide range of materials that can be deposited with this method. Although the method itself is inherently simple, consisting of only a heated wire within a vacuum chamber where reactive gases pass through, the actual chemistry that governs the deposition reaction is still under debate. The standard growth model attributed to Masuda [1], Gallagher [2], and Perrin [3] (the MGP model) suggests that the fundamental limitation to high deposition rates of electronics quality material is the surface diffusion of the silyl (SiH_3) radical. The model theorizes that as a silyl radical diffuses near the surface of the growing film it can bond to a surface bonded hydrogen and remove it; or it can bond to a vacancy, thus adding to the growing film. It is this hydrogen abstraction by radicals that is postulated to be the rate limiting and defect-reducing step. However, this hydrogen abstraction reaction is also the subject of debate over the deposition chemistry.

The MGP model is used extensively to explain plasma enhanced chemical vapor deposition (PECVD) in literature; however the model doesn't account for the empirical evidence that high quality materials are formed under low pressures with high ion bombardment levels using remote plasma processes [4-6]. Ions are always present in plasma discharges, as they are the end product of electrons ionizing the gases present in the plasma zone of the reactor; however there are no ions present

in HWCVD processes. Ions have been shown to be important in PECVD processes, where low ion energies and high ion densities have produced higher quality materials, stimulating a shift from radio frequency (rf) PECVD to VHF PECVD processes where more ions with lower energies are produced than conventional rf-PECVD. How does one account for the improvement in film qualitiy that this increased ion bombardment makes with the MGP model?

The discrepancy between the empirical data presented in literature and the basic theory of the MGP surface diffusion model is of great importance when studying high deposition rate processes. HWCVD has produced materials with photosensitivities in the 10^5 range and Urbach energies below 50 meV [7-9], typical of high quality hydrogenated amorphous silicon, without any ion bombardment at very high growth rates. PECVD has produced materials with Urbach energies below 45 meV and photosensitivities in the range of 10^6, albeit at a fraction of the growth rate. Is the energy provided from the ions impacting the film surface enough to produce this difference in material quality?

What is the role of ions in the growth reactions of a-Si:H and a-(Si,Ge):H? Does ion bombardment result in improved film quality due to the energy the ions impart to the surface of the growing film, or does PECVD produce better materials because it is a more mature technology? Some researchers speculate that the absence of ion bombardment makes HWCVD superior because the energetic ions are not disrupting the growth of the film, while others conclude that ions improve the material when a high density of low energy ions impinge upon the growing film's surface. It is clear that the effect of ion bombardment during film growth of a-(Si,Ge):H needs to be studied systematically where ion bombardment can be turned off or on with all other variables held essentially constant.

1.2: Standard Growth Model

The standard growth model for PECVD and HWCVD is the model attributed to Masuda, Gallagher, and Perrin [1-3], otherwise known as the MGP model. The MGP model is used widely in literature to describe PECVD processes; however the effects of ion bombardment are not addressed in the model.

Silyl radical

Silane product

Radical binds to surface hydrogen

Substrate
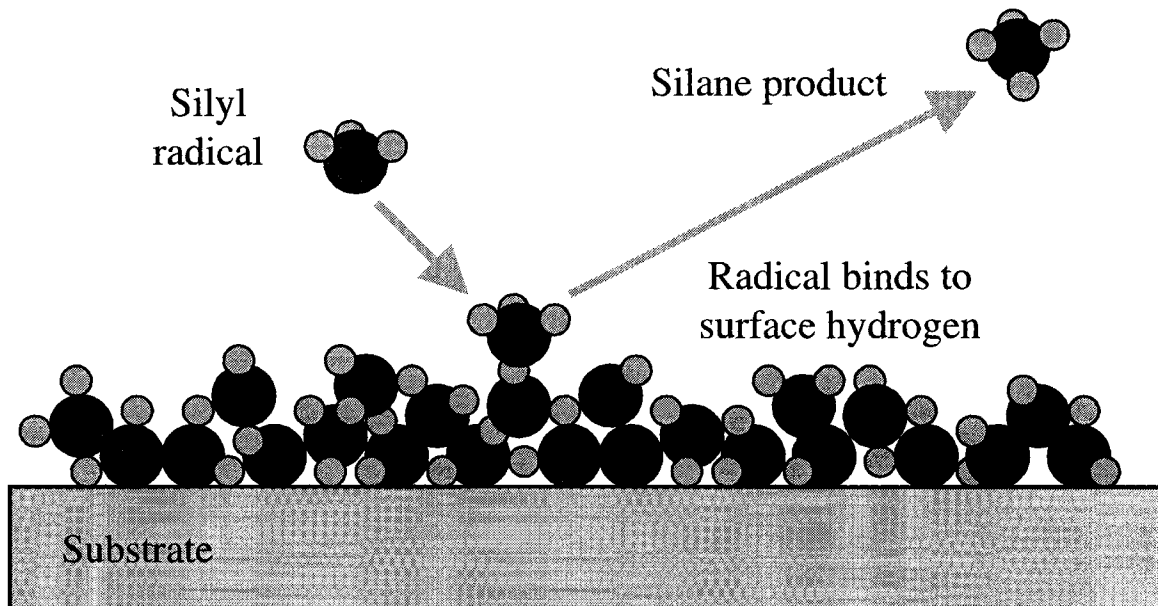
Figure 1.1: Hydrogen abstraction reaction as postulated by the MGP model

The basic premise of the MGP model is that hydrogen is abstracted by a silyl (SiH_3) radical creating a vacancy at the surface of the film. This vacancy is then filled by the addition of another silyl radical to the unbound electron left by the abstracted hydrogen. Figure 1.1 shows the hydrogen abstraction by a silyl radical and figure 1.2 shows the addition of another silyl radical to the vacancy. The MGP

Silyl
radical

Radical binds to
surface, adding to film

Substrate
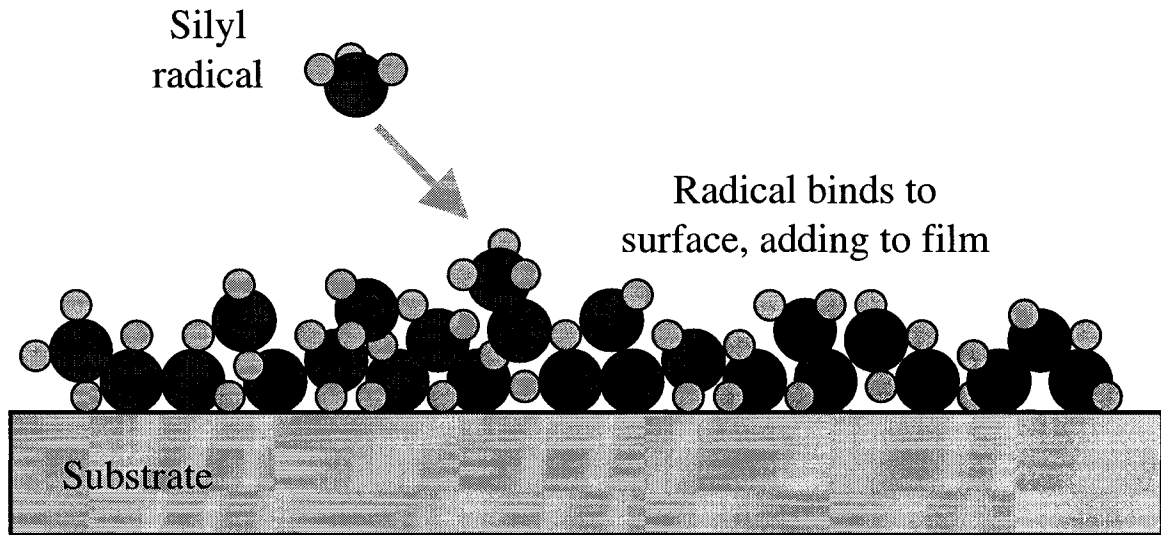
Figure 1.2: Film growth reaction from the MGP model

deposition chemistry model is then reliant upon the surface mobility of the SiH_3 radical and the effectiveness of hydrogen abstraction by the silyl radical.

Experimentally, this model fits the preponderance of evidence available. There are numerous studies that correlate the surface reaction kinetics through various sticking coefficient models and lend credence to the theory [2,3, 10,11]. In addition to the sticking coefficient results, studies have shown that the model is consistent with the smooth surfaces requiring high surface diffusion of the ad-radicals that are observed when depositing hydrogenated amorphous silicon and germanium alloys [10]. Also given as support to the MGP model is the observation that GeH_3 or SiH_3 cannot insert directly between a Si-Si, Ge-Si, or Ge-Ge bond [10], necessitating a two-step model.

1.3: Previous Ion Bombardment Studies

Very few studies on the role of ion bombardment in deposition have been reported, and of those studies that have been published in literature, many are concerned with triode biasing schemes where an rf-PECVD reactor has an independently biased mesh screen installed between the anode and cathode. Studies of ion bombardment in literature are also mainly concerned with amorphous silicon exclusively, paying no regard to a-(Si,Ge):H, which is a more sensitive material to ion damage due to the decreased Ge-H bond energy as compared to Si-

Photosensitivity as a function of V_{pol} (V)
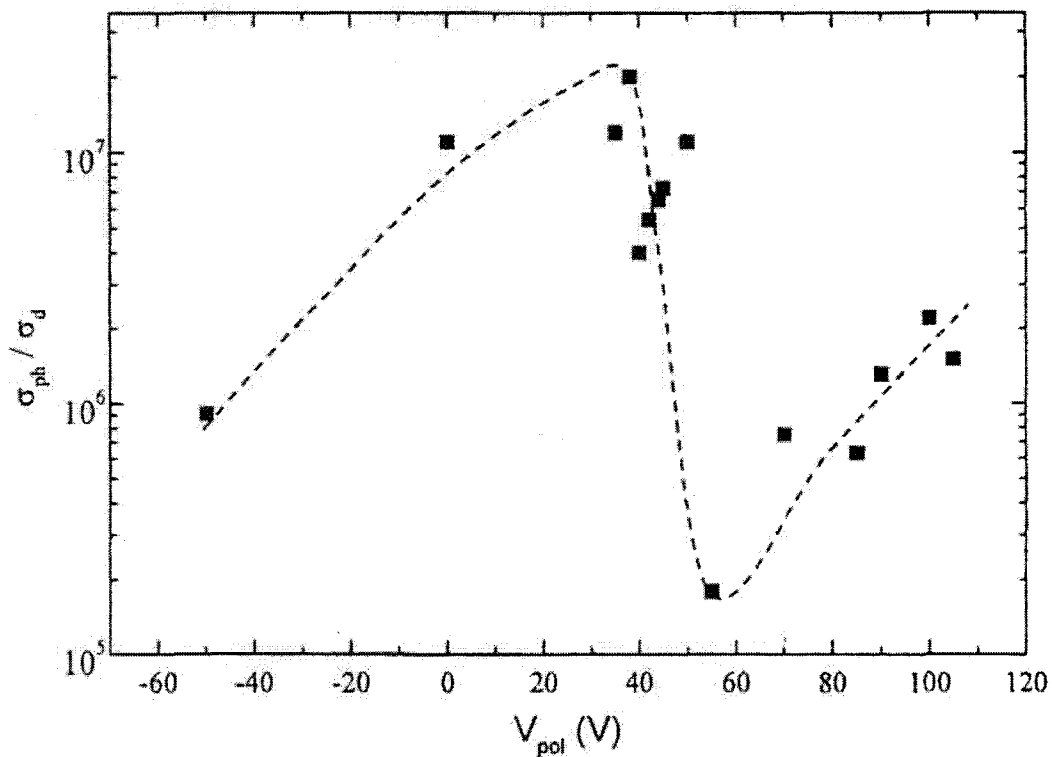
Figure 1.3: Photosensitivity vs. the mesh bias potential [12]

H. Studies using the mesh bias potential method of adjusting ion bombardment are, however, fraught with ambiguity as the plasma regime and chemistry can change dramatically as the triode mesh potential is varied.

In reports published by Aguas, et al [12], an interesting phenomenon is observed with the variation of the mesh potential. The results of these experiments indicate that as ion bombardment energy increases, the material properties improve to a point, after which a degradation is observed. In figure 1.3, a plot of photosensitivity versus the V_{Pol} parameter, a measure of the mesh bias potential,

Microstructure as a function of V_{pol} (V)
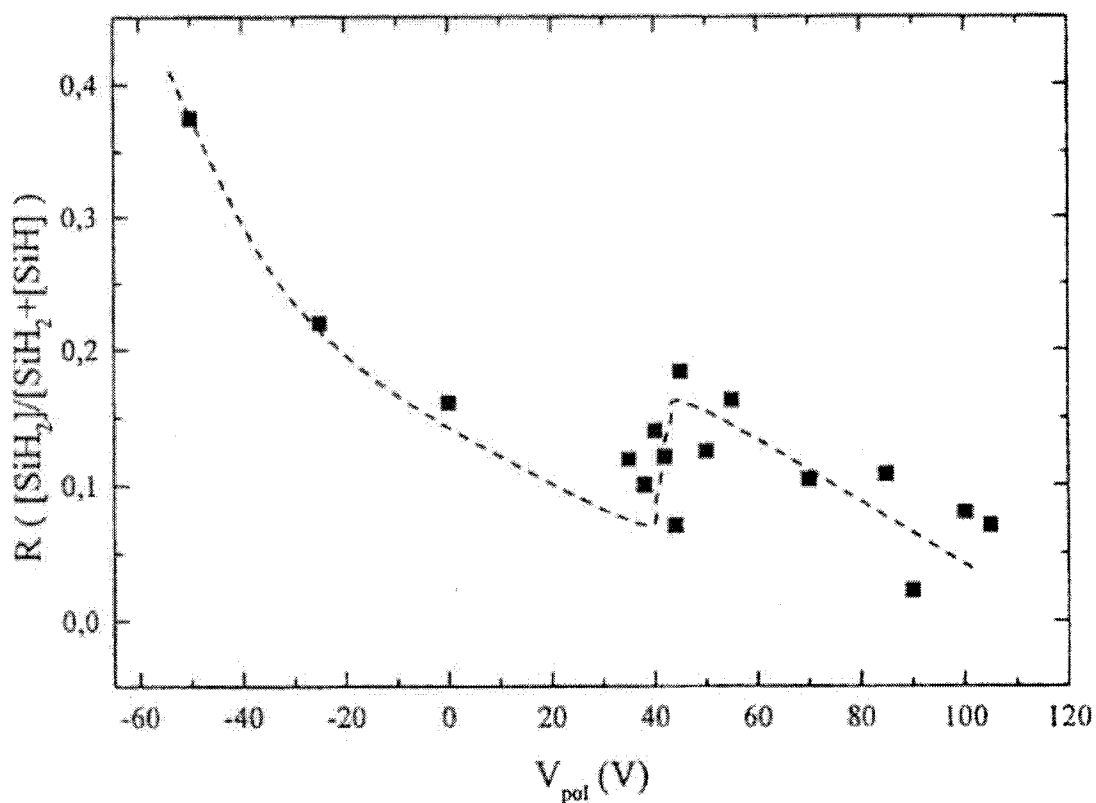
Figure 1.4: Hydrogenated amorphous silicon microstructure vs. V_{pol} [12]

one sees a great improvement in photosensitivity until a V_{Pol} of ~40 V. After

reaching a peak value of ~2x10^7 at 40 V, the photosensitivity drops and never

reaches the same value again. A similar phenomena is seen with the variation of R

as a function of V_{Pol}, shown in figure 1.4, where R decreases with increasing V_{Pol}

until V_{Pol} = 40 V. After the mesh potential reaches the 40 V, the microstructure

increases and then proceeds to decrease again. Incidentally, as V_{Pol} increases, the

ion bombardment energy also increases, and the decreasing microstructure after

~50 V may be attributed to diminished hydrogen content in the material, however

that data was not presented.

These results suggest that ion bombardment is beneficial to the deposition of

amorphous semiconductors, as increased ion bombardment energy improves the

material to a point, then diminishes its properties. Ion bombardment can be viewed

as a source of energy to the growing film, like substrate temperature, and like

substrate temperature, an increase in value will improve the material to a certain

point, then a degradation of material properties will occur.

Other research groups have taken different approaches to the ion

bombardment question. One group deposited a-Si:H on independently biased and

heated electrodes placed between the anode and cathode in a PECVD reactor [13].

This group showed that increasing ion bombardment energy would improve

materials grown at low substrate temperatures and degrade materials deposited at

higher substrate temperatures [13]. The effect of ion bombardment has been

interpreted as improving the diffusion of hydrogen at the growth surface that in turn

promotes hydrogen abstraction. This increase in hydrogen abstraction by radicals or ions then promotes the homogeneous bonding of SiH_3 radicals and the properties of the resulting material [14]. This theory can describe the results shown earlier where the material first improves, then deteriorates, as that material sees the abstraction of hydrogen first as beneficial to allow better silyl diffusion and bonding, then as the amount of hydrogen abstraction increases, the bonding of silyls cannot keep up, and dangling bond defects are introduced into the material. The result of the increased dangling bond density is seen both as diminished photosensitivity, photoconductivity, and as lower microstructure with diminished hydrogen content.

The beneficial effects of ion bombardment have been used by many to fabricate amorphous silicon devices on thin polymer sheets that cannot withstand the temperatures used for conventional deposition on glass substrates. One group of researchers from the jet-propulsion laboratory studied high ion-bombardment conditions for a-Si:H deposition to be used for thin film transistors [15]. This group found that ions with energies less than 10 eV were enhancing surface diffusivity and hydrogen abstraction, as the resulting TFT's from this material were of a quality similar quality to those produced by convention deposition on glass substrates [15]. In addition, these researchers observed the microstructure resulting from different ion bombardment conditions for substrates at room temperature. The results showed a decrease in microstructure as the plasma power density of the rf-PECVD reactor increased. This result again points to the benefits of ion bombardment as ion flux is shown to improve the surface reactions of the deposition, through surface mobility improvements.

In other research where high ion bombardment conditions are used in rf-PECVD reactors, researchers observed improved microstructure again, improved photoconductivity at low substrate temperatures, and even improved photoconductivity in a-SiGe:H alloys [16]. The over-bombardment effect was seen also in a-Ge:H deposition [17], where lower ion energies showed microstructure improvements and photoconductivity increases, however the very high ion energies used in the researcher's argon ion beam set up created materials with very high defect densities and large absorption band tails [17].

Much of literature is devoted to showing how ion bombardment improves surface diffusion; however it is also postulated that ions can remove weakly bound hydrogen and thus create sites for the addition of new silyl radicals. Dalal postulates that hydrogen bound at the surface, and just below, can be removed by hydrogen ions [4]. Helium and argon ion bombardment is also discussed, where these inert ions are postulated to form dangling bonds at the surface to promote the addition of new silyl radicals, whereas the hydrogen ions penetrate deeper to remove bulk hydrogen and reduce voids and microstructure of the material [4]. The recent interest in VHF-PECVD deposition is also examined as he surmises that the lower energy ions help the surface reactions more than the higher energy rf-PECVD ions. The rf-PECVD ions generally require high pressures or triode screens to reduce their energy to levels where their bombardment becomes beneficial, as discussed earlier in this section. The VHF plasma also generates a higher density of ions, making the total number of ions impinging the surface greater, thus the benefits of low energy ion bombardment is more uniform. The current trend seen in the

switching to VHF from radio frequency plasmas is tied in to the benefits of ion bombardment.

Prof. John Robertson at Cambridge University uses thermodynamics and reaction kinetics to propose a model that relates material growth including ion bombardment, and the resulting dangling bond density, and thus the material quality. He postulates, like Dalal, that hydrogen removal is the key step in the deposition of high quality amorphous material deposition [18]. Robertson proposes that in addition to hydrogen abstraction by the silyl radical, atomic hydrogen can remove surface bound hydrogen, and that hydrogen ions can penetrate into the film to remove subsurface hydrogen, as shown in figure 1.5. The process of removing
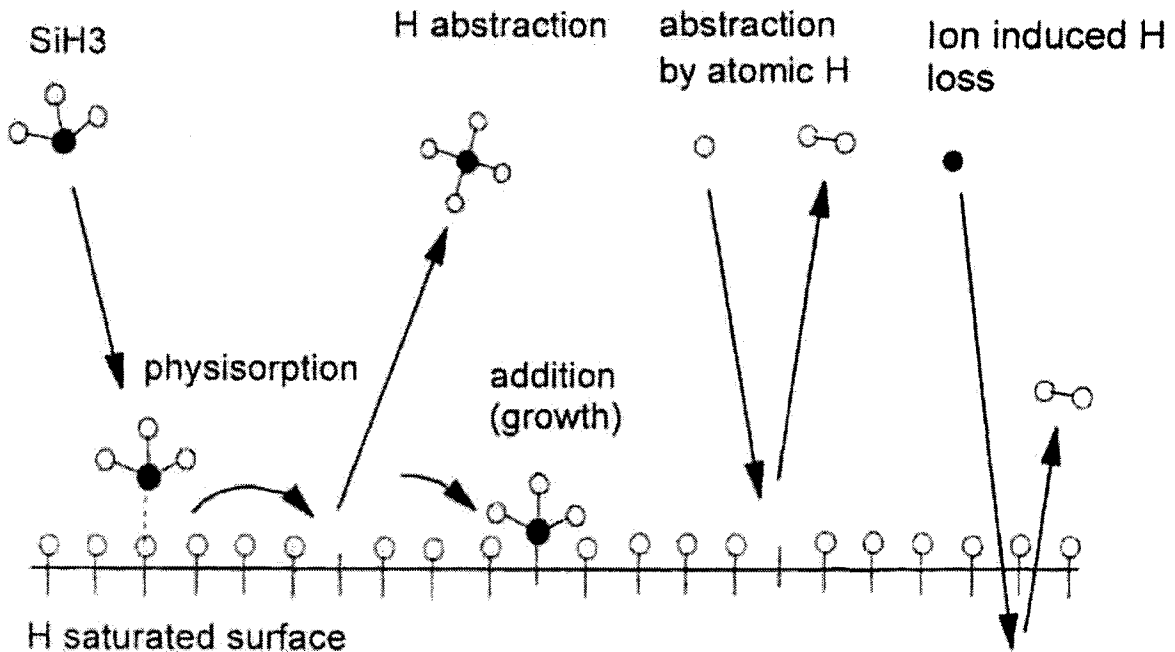
Figure 1.5: Hydrogen removal methods as postulated by J. Robertson [18]

excess hydrogen by ion bombardment is complex, as it depends upon the internal distribution of weak bonds. The weak bonds are generally thought to be the limiting factor when determining the overall defect density of the material, as these weak bonds will decompose to segregate the hydrogen and silicon atoms in a spinodal decomposition where the most energetically favorable arrangement is not a random distribution, but one grouped by atom. The hydrogen ions react with the weakly bound hydrogen and form a H_2^* complex that can then easily diffuse through the film to the surface [18] as it has a lower free energy transition state than a single hydrogen atom does. The driving force behind the diffusion to the surface of the film is the spinodal decomposition resulting from the chemical energetics of the system, and the fact that the complex diffuses with less energy cost than a single hydrogen atom as the complex is not attempting to bind as it travels through the material [18]. In this work experimental evidence is provided that supports this model, as reactive H^+ ions produce superior materials compared to He^+ ions.

All of the literature reviewed here shows that ion bombardment plays a role in the deposition chemistry of amorphous semiconductors. The ion bombardment studies have shown definite correlation between the ion densities and energies, the resulting material quality; and also shown a theoretical reason for the benefit. In addition to the studies of ion bombardment effects, many researchers have used high ion bombardment conditions to produce materials of very high quality for many applications. Clearly ion bombardment must be included in any reasonable model for the deposition of amorphous semiconductors in a plasma enhanced chemical vapor deposition environment.

1.4: Research Objective

The objective of this research is to study the effects of ion bombardment during growth on the physical properties of the resulting material. In examining the effects of ion bombardment, modifications to the MGP model will be suggested that will attempt to reconcile the standard model with the fact that photovoltaic grade materials are routinely deposited under high ion bombardment conditions. In addition, the model suggested by Robertson is supported by this research, and it is shown that neutral ions also promote the growth of high quality a-(Si,Ge):H materials of high band-gap.

In addition to amending the MGP model, this research intends to successfully deposit the first a-(Si,Ge):H materials using the combined hot-wire ECR technique and prepare the first ever photovoltaic devices containing "intrinsic" layers prepared by HW-ECR. Materials deposited at growth rates above 1 Å/s are examined, as HWCVD is a high growth rate process. The materials deposited in this work are characterized by measuring photoconductivity, dark conductivity, the light/dark conductivity ratio, activation energy, Urbach energy, sub-band gap absorption coefficient, film thickness, growth rate, SCLC mid-gap defect density, and the FTIR microstructure. In addition, the first ever photovoltaic devices with i-layers deposited by the combined hot-wire ECR plasma were fabricated and characterized by measuring the illuminated J-V curve and both biased and unbiased quantum efficiency spectra.

CHAPTER 2: SAMPLE PREPARATION

Samples were prepared using both hot wire chemical vapor deposition (HWCVD) and a novel process using HWCVD and a remote electron-cyclotron resonance (ECR) plasma. Each of these two deposition techniques were performed in the same reactor yet have unique deposition chemistries and parameters, as discussed below.

2.1: Hot Wire Chemical Vapor Deposition

HWCVD is an emerging technology for the deposition of hydrogenated amorphous silicon and its group IV alloys [19]. Recent interest in HWCVD was sparked by reports from Matsumura, who deposited amorphous silicon using tungsten filaments and silane gas to produce electronics grade material [20]. Matsumura showed that by using the relatively simple HWCVD process, he could produce a-Si:H with properties near radio frequency (rf) plasma enhanced chemical vapor deposition (rf-PECVD) materials, at growth rates approximately 10-20 Å/sec [20]. Also, it has been shown that by using suitable dopant gases, n or p type material [20], a-(Si,Ge):H [21], or microcrystalline silicon [22,23] can be grown by HWCVD. These attributes make HWCVD desirable for photovoltaic production because a single reactor operating at a high deposition rate can be used for the entire device fabrication [23].

2.1.1: Decomposition Reactions

HWCVD chemistry begins at the hot filament, generally composed of tungsten (W) or tantalum (Ta). The catalytic filament is resistively heated by passing a current through the thin wire, and shows an increasing reaction probability with

silane as the filament temperature (T_{fil}) increases until approximately 1800°C at chamber pressures around 10 mTorr [24]. Under these conditions with T_{fil} above 1800°C, the decomposition reaction probability of SiH_4 reaches a maximum value as T_{fil} increases. The filament is never used at temperatures very near its melting point as filament failure and unintentional doping of the silicon may occur, therefore imposing a maximum operating T_{fil}.

When operating a HWCVD reactor with T_{fil} in the range between 1800°C and the maximum operating temperature, silane undergoes complete thermal decomposition as shown in equation 1 below [24]. The silane gas contacts the heated filament and the thermal energy transferred to the gas molecule breaks all four hydrogen-silicon bonds producing the

$$SiH_4^{(g)} + filament^{(s)} \rightarrow Si^{(g)} + 4H^{(g)} + filament^{(s)} \qquad (2.1)$$
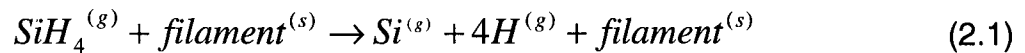
reaction shown in equation 2.1. When the filament temperature is less than 1800°C, the reaction at the catalytic filament becomes much more complicated as the release of Si and hydrogen from the filament does not occur as readily, and silicides containg silicon and the filament material can be formed on the filament [24].

2.1.2: Gas Phase Reactions

After the molecular silicon and hydrogen are released from the decomposition of silane, two distinct classes of gas phase reactions occur: radical-silane and radical–radical reactions. Gallagher proposes that the main radical-silane reaction responsible for high quality films at typical deposition pressures is molecular hydrogen combining with silane to form hydrogen gas and SiH_3, as shown in equation 2.2 [24]. This explanation is consistent with results from deposition studies

$$H + SiH_4 \rightarrow SiH_3 + H_2 \qquad\qquad (2.2)$$

$$Si + SiH_4 \rightarrow Si_2H_2 + H_2 \qquad\qquad (2.3)$$

$$Si + SiH_4 \rightarrow SiH + SiH_3 \qquad\qquad (2.4)$$

$$Si + SiH_4 \rightarrow Si_2H_4 \qquad\qquad (2.5)$$

$$Si + SiH_4 \rightarrow Si_2H_2 + H_2 \qquad\qquad (2.6)$$

comparing hydrogen diluted and non-diluted silane gas feeds, where the material made from the diluted gases is nearer to the amorphous/microcrystalline phase border, and therefore has lower defect densities making it a higher quality material [25]. These results confirm what one would expect in excess hydrogen, where the reaction of equation 2.2 predominates as hydrogen gas thermally dissociates upon contact with the filament as well, providing an abundant supply of atomic hydrogen radicals. Other radical-silane reactions occur as well, as shown in equations 2.3 through 2.6, which can provide undesirable radicals for high quality film deposition, such as SiH, SiH_2, and Si_2H_4 [4,24]. The incorporation of SiH, SiH_2, and Si_2H_4 into a growing film results in dangling bond defects that are deleterious to the electrical properties of the film. When the chamber pressure is high, higher silanes such as Si_3H_6 can be formed when the products of equations 2.3 through 2.6 combine with SiH_4. These multiple silicon molecules have little surface mobility and lead to the introduction of defects if incorporated into the film, or dust formation that wastefully consumes the feed gases [24].

The PD product is a parameter used to characterize the reactions for a given reactor setup, where P is the chamber pressure and D is the distance from the filament to the substrate surface [19]. In the work by Molenbroek, et. al. [19], the authors concluded that a PD product of 10 to 15 mTorr-cm yielded the highest

quality material at high growth rates in a HWCVD reactor having a filament to substrate distance of 1-1.5 cm. The PD product describes the gas phase reaction progression after thermal dissociation, as the higher the product value more reactions can occur in the gas phase between the filament and the substrate, and conversely the lower the PD product, the fewer reactive collisions can occur.

2.1.3: Surface Reactions

The third class of reactions in HWCVD processes occur on and just beneath the growing film surface where weakly bonded hydrogen and/or silicon is removed or rearranged [16]. In these reactions there has to be enough energy to break the ~3 eV Si-H bonds and release excess bonded hydrogen so it can diffuse out of the material and lower the overall hydrogen content of the film. In high growth rate processes, such as HWCVD, a high substrate temperature provides enough thermal energy to break weak hydrogen bonds and produce electronics quality materials with 5-10 at.% hydrogen content. Higher substrate temperatures also provide greater surface mobility of SiH_3 radicals, promoting more consistent film growth, as in this process there are no ions to add energy for hydrogen abstraction or silyl diffusion.

2.2: Electron Cyclotron Resonance Plasmas

ECR plasmas are ubiquitous in semiconductor manufacturing today, and as a result have been described and discussed repeatedly in literature [27-33], and will only briefly be discussed here. The ECR condition is predicted by Maxwell's equations and is caused by microwave radiation being directed perpendicular to a static magnetic field. This arrangement causes electrons to both rotate and move back and forth linearly, producing a dense cloud of energetic electrons moving in a vibrating helical trajectory that form ionized radicals when they contact gas

molecules in the same volume, creating the ECR plasma. In a remote plasma system, the ionized radicals are then directed toward the substrate through a stream of intrinsic gases such as silane or germane to form reactive species. The plasma species can also collide with the growing film surface imparting energy to break bonds such as the deleterious dihydride bonds, or rearrange silicon atoms. It is this function of ECR plasmas that is sought in this study to improve the film properties at low temperatures.

When using ECR plasmas to provide ion bombardment during film growth, it is imperative to limit the ion energy from 2-5 eV to avoid damaging the film. ECR plasmas allow for the controlling of ion energy that reaches the substrate by controlling microwave power, magnetic field strength, and the chamber pressure. The use of low energy ion bombardment has been shown to improve photoconductivity in HWCVD prepared films [34,35], and its effects on other aspects of a-(Si,Ge):H is investigated further in this study.

2.3: Combined ECR-HW CVD Reactor

For this study, a remote ECR plasma unit was coupled with a HWCVD reactor as shown in figure 2.1 and in Appendix 1. An ECR plasma and catalyzing filament have been coupled together in previous investigations at Iowa State University [34,35], however there are some notable differences between the original system and the one shown in figure 2.1 below, such as an increased filament to substrate distance and a new gas outlet behind the substrate holder.

In the reactor system, a 2.45 GHz microwave source and three stub tuner by Sairem of France was used to provide the microwave energy for the ECR plasma. The microwave power was varied between 50 and 100 W, however the settings on the tuner were seldom adjusted during the experiment. The quartz window used to
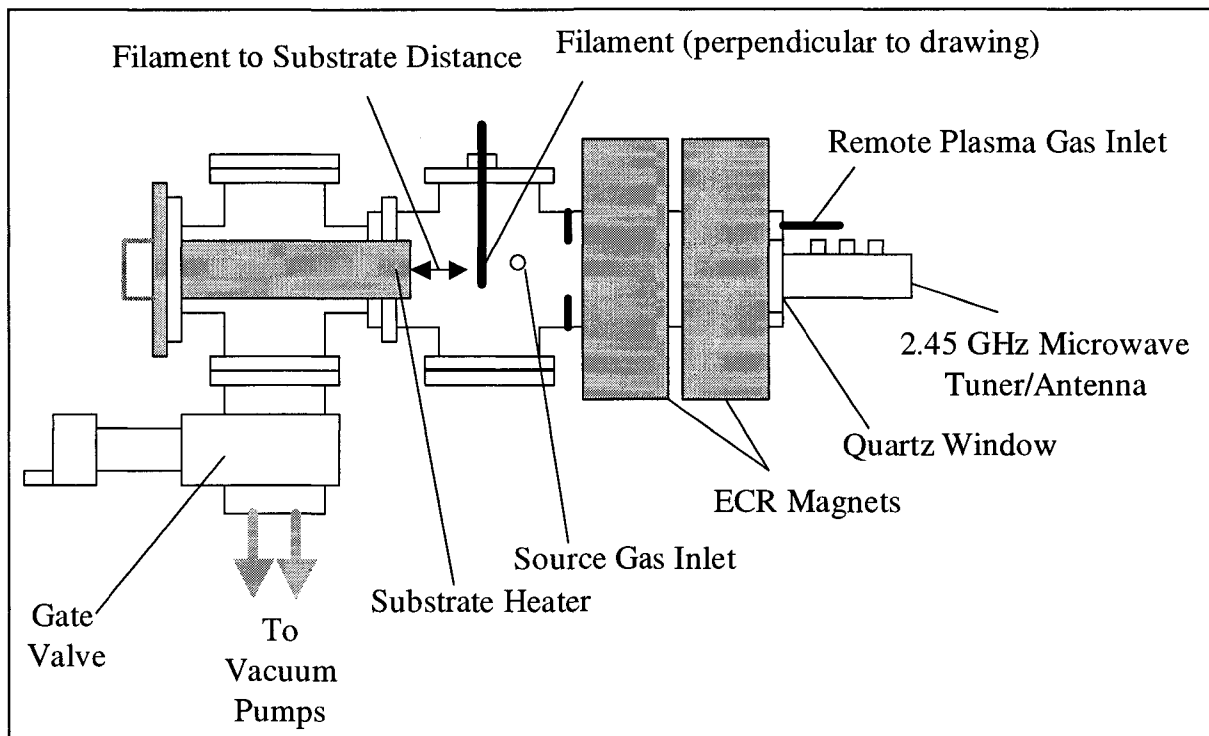
Figure 2.1: Schematic of Combined ECR-HW CVD

maintain vacuum inside while allowing microwaves to enter the deposition chamber was cleaned regularly when using the combined ECR-HW CVD deposition process. The cleaning ensured consistent plasma conditions from deposition to deposition and reduces heating from microwave absorption by the silicon coating on the quartz.

Two stationary magnets mounted around an 8 in. stainless steel tube supply the magnetic field required for the ECR condition to be met, as shown in figure 2.1. The magnets consist of a large wire coil powered by a DC constant current power supply with adjustable output. The ability to adjust the current output enables control of magnetic field that directly affects the plasma ion density.

The gases used during deposition can enter from two areas in the reactor. The silane used to supply the silicon ultimately incorporated into the growing film

enters the reactor near the catalytic filament, as shown in figure 2.1. Other gases such as He or H_2 that become ions in the plasma enter through a gas diffusing ring that surrounds the quartz window near the Sairem tuner. By segregating the gases, a greater amount of control over ion species and energy can be attained than with a single gas injection point.

The catalytic filament is located in a vacuum cross separated from the plasma generation region by a restricting orifice that shapes the plasma into a diverging cone. The filament is oriented parallel to the substrate supported by two stainless steel rods each threaded into a copper vacuum feed-through. The filament is composed a 40 cm length of either tungsten or tantalum wire having a 0.5 mm diameter wound into a helix and spans a 7 cm distance. The filament to substrate distance of the reactor is non-adjustable and measures 10.5 cm, which is considerably longer than most other HWCVD reactors. This large distance minimizes substrate heating through radiation.

A Watlow PID temperature controller connected to an Omega thermocouple mounted in a recess machined into the substrate holder control the temperature of the substrate. The PID controller supplies power to a 120 V, 600 W Chromalox disc heater mounded outside the vacuum on the substrate holder and insulated from the ambient air temperature by silica board. The substrate holder itself is mounted at the end of the reactor, as shown in figure 2.1. The substrate is held firmly against the substrate holder by a stainless steel mask covering the entire end of the holder except for a 1 in.^{2} square.

The deposition chamber is evacuated by a Pfifer-Balzer turbomolecular pump backed by a mechanical backing pump with a continuous N_2 purge to prevent toxic gas accumulation in the ventilation system. A gate valve directly ahead of the turbomolecular pump controls chamber pressure during deposition and a small

mechanical pump with a separate valve into the chamber accomplishes chamber roughing. The vacuum system provides a background pressure in the order of 10^{-7} Torr while typical deposition pressures are from 100 to 1 mTorr.

2.4 Thin Film Deposition Methods

Thin film depositions require a high level of care be taken during processing to ensure a consistent and high quality result. Over many years of amorphous hydrogenated silicon deposition at the MRC, a general procedure has been developed for ECR-PECVD thin film growth to ensure repeatability of results. When using HWCVD or HW-ECR CVD, an almost identical process was followed.

All substrates were cleaned in a similar manner, whether 7059 Corning glass for electrical characterization or double side polished silicon wafers for hydrogen content and microstructure determination. The substrates are first boiled in acetone for 15 minutes to remove organic compounds, such as waxes and oils that adhere to the materials after handling. A 15-minute ultrasonic bath in methanol then removes the traces of acetone from the first cleaning step and most other compounds that may still be adhered to the substrate. The substrates are stored in methanol until required for use, and then blown dry with nitrogen immediately before installation into the substrate holder and insertion into the reactor.

After the dried substrate is loaded into the reactor system, a series of purges is undertaken to remove any moisture that may have entered the system during the brief time it was opened to the atmosphere. The purges consist of 10 nitrogen purges that flush any oxygen from the system, then ten silane and hydrogen purges that remove moisture, and finally five hydrogen purges to rinse the heavy silane molecules out of the system.

While purging, the substrate temperature is ramped up to fifty degrees beyond the deposition conditions, to ensure complete heating of the entire thermal mass associated with the substrate holder and mask. After the controller has damped the temperature variations and indicates the initial set point as the substrate temperature, the set point is decreased to the desired deposition condition. This overheating also provides an increased thermal loading of the stainless steel substrate holder to ensure heat conduction to the substrate surface.

As the substrate cools to the correct temperature for deposition, an ECR discharge consisting of the same gas ratio as the actual deposition layer is deposited on the interior reactor surfaces to seal in any atmospheric contaminants, such as oxygen, introduced when the new substrate was loaded into the chamber. To ensure that the substrate itself is not coated with this dummy layer, a shutter is mounted on a magnetic linear motion feed-through is placed in front of the substrate holder. This dummy layer is deposited the under the same plasma conditions for each band-gap material for at least thirty minutes to reduce systematic error from contamination.

After the dummy layer is complete, the hot wire filament must be cleaned before it can be used in HWCVD. The filament-cleaning step consists of flowing hydrogen at 25 sccm into the chamber via the intrinsic line while heating the filament to approximately 2200°C for five minutes at a pressure of 15 mTorr. In addition to removing the dummy layer from the filament surface, any silicides that formed at the cooler ends of the wire during the previous deposition are also etched away, improving the subsequent film's properties, as postulated by Ishibashi [36].

After the filament cleaning procedure, the gas flows, plasma conditions, and the catalytic filament current to be used during deposition are set and the reactor is allowed to come to steady state before the shutter is opened to begin deposition.

After the shutter is opened and the timer triggered, the reactor conditions are checked periodically during the deposition time to ensure consistency. The actual deposition time for each sample varies so that a film of ~ 1 μm thickness is grown. The deposition is stopped by first closing the shutter, and then turning off the tantalum filament and the plasma if necessary. The PID substrate temperature controller is set to ~30°C and the flowing gases are shut off and all lines purged. The chamber is then filled with silane and hydrogen, in approximately equal parts, to a pressure of 1 Torr to aid in cooling of the film. After the film is cooled to below 150°C, as indicated by the thermocouple, the silane-hydrogen is evacuated and one nitrogen purge performed before filling the chamber with nitrogen up to atmospheric pressure for sample removal.

2.5: Device Fabrication

Both p-i-n solar cell devices and n-i-n devices for use in characterizing the mid-gap defect density by the space-charge limited current (SCLC) technique were fabricated in this study. The fabrication of each of these devices follows a similar method, where a conventional PECVD n^+ layer is deposited on stainless steel substrate, the intrinsic layer (or layers) is deposited by HWCVD or HWECR, and then the final n^+ or the p^+ top layer is deposited by ECR plasma deposition.

2.5.1: SCLC n^+-i-n^+ device fabrication

The n^+-i-n^+ devices used for SCLC characterization are essentially thin intrinsic material layers with whole surface contacts on the top and bottom of the layer. The contacting layers above and below the intrinsic material being characterized are very highly doped so that the conduction band is nearly incident with the Fermi level to allow for transport of electrons into the bulk of the material.
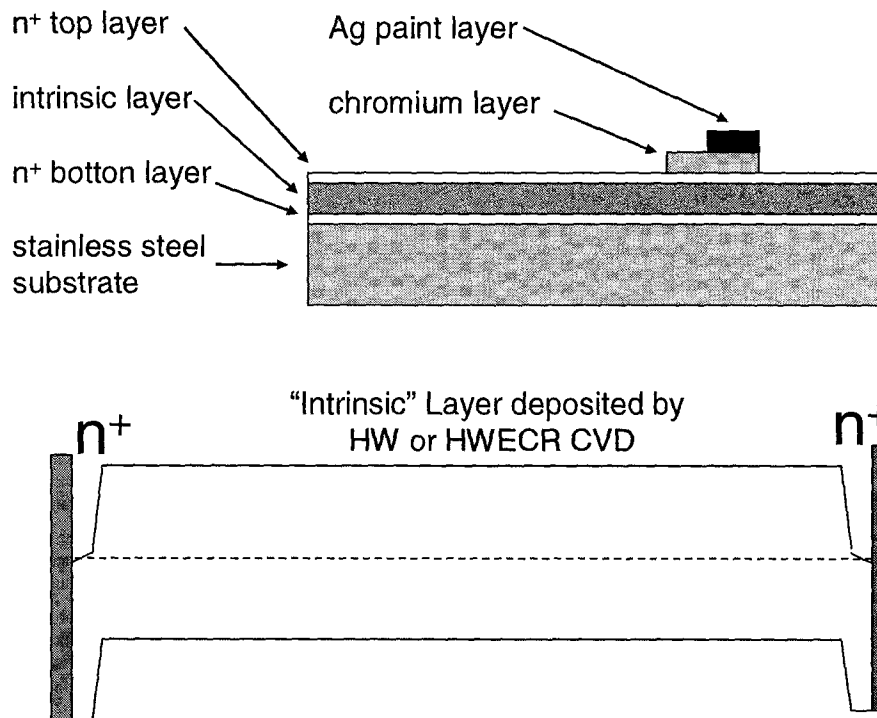
n+ top layer

intrinsic layer

n+ botton layer

stainless steel
substrate

Ag paint layer

chromium layer

n^+ "Intrinsic" Layer deposited by
HW or HWECR CVD n^+

Figure 2.2: Schematic and non-biased energy-band diagrams for a typical n^+-i-n^+ device

used for SCLC midgap defect density of states determination

Figure 2.2 shows a schematic representation of the device and a sample band

diagram. In the band diagram notice the ends of the devices where the Fermi level,

denoted by the dashed line, is coincident with the conduction band of the n^+ layer. If

hole trap states were to be examined by injecting holes into the material a p^+-i-p^+

device would be used.

These devices are fabricated by first obtaining an n+ layer deposited on a

stainless steel substrate. The stainless steel substrates are cleand in the same way

that the 7059 Corning glass is prepared, with an acetone boil followed by a methanol

ultrasonic rinse. The substrates are stored in methanol until used for deposition,

when they are blown dry with dry nitrogen gas.

After drying the substrate, it is loaded into the VHF PECVD reactor where an amorphous silicon layer doped with phosphorus is deposited by striking a 10 W plasma in an atmosphere containing silane, hydrogen, and phosphine gases. After deposition is complete, the substrate and film is removed from the reactor after it has cooled to below 100°C, and placed directly into a methanol bath. The methanol keeps oxygen from reacting with the silicon in the film and forming a thin oxide layer.

The substrate and thin n^+ film are then transferred into the HW-ECR reactor for deposition of the intrinsic layer. The sample is blown dry with nitrogen again before being loaded into the vacuum system. The intrinsic layer deposition is performed just as material depositions are, with the exception that the substrate temperature offset is lower with stainless steel that with the 7059 glass.

Once the intrinsic layer deposition is complete, the device is allowed to cool to ~100°C in a hydrogen and silane atmosphere and then it is removed and again placed in a methanol bath for storage until the top layer deposition can be completed. The top layer is the final layer deposited using PECVD and is deposited using silicon and germanium if the intrinsic material is a-(Si,Ge):H, otherwise due to conduction and valence band mismatch between a-Si:H and lower band-gap a-(Si,Ge):H, the SCLC curves exhibit non-symmetrical behavior and are not reliable for determining the mid-gap defect density of the material. The top layer material is deposited using a mixture of silane, germane, hydrogen, and phosphine gases to grow a highly doped amorphous silicon-germanium alloy where the conduction band is very near the Fermi level in that material. Circular chromium contacts are then deposited on the top layer after top layer deposition is completed to finish the device for use in SCLC characterization.

2.5.2: Photovoltaic p⁺-i-n⁺ device fabrication

The deposition of photovoltaic devices for this research and the n-i-n devices for SCLC and are essentially the same, with the bottom n^+ layer and intrinsic layers being deposited identically. The difference between the two device types comes in the top layer and contacts used on each device.

The fundamental behavior of the devices is very different, however. The SCLC device serves simply as a charge injection device where a rectifying contact forms a diode that can be analyzed to determine the amount of trapped charge in the bulk layer. The photovoltaic device is different in that it generates carriers and needs to collect each carrier type to generate current to power an outside circuit.
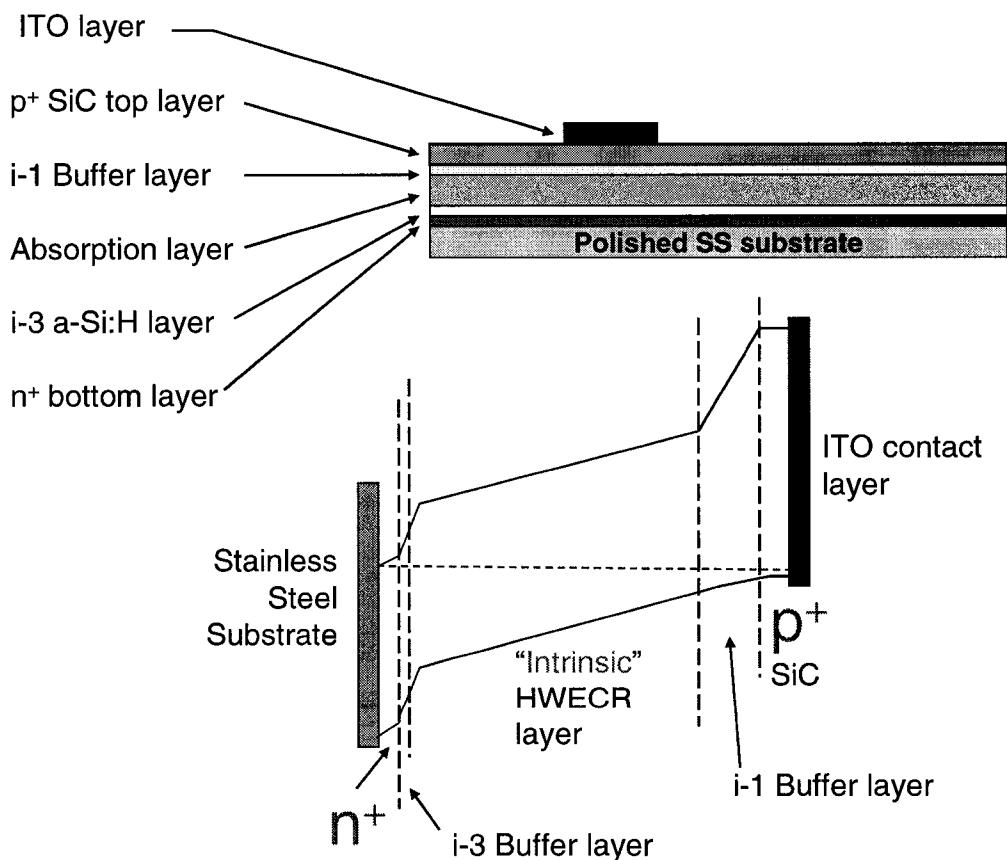

Figure 2.3: Schematic and energy-band diagrams for a typical p⁺-i-n⁺ photovoltaic device

Photovoltaic device design is very complex as there are many parameters that can be varied to improve the carrier generation and collection from the available solar spectrum. In fact, the motivation behind depositing the various band-gap silicon germanium is the use of a graded band-gap absorption layer, which promotes carrier collection, and the ability to match the absorption spectrum to the solar spectrum. For the devices examined in this research, only the simplest of devices were fabricated, with a single band-gap intrinsic layer, an n^+ bottom layer with thin a-Si:H buffer, a standard a-SiC:H graded buffer layer, the research group's standard p^+ top layer, and ITO top contacts, as shown in figure 2.3. Also shown in this figure is the band structure of the device, which promotes carrier collection while reducing top surface recombination through the graded silicon carbide top p^+ layer. This top layer is also of a band-gap larger than the intrinsic layer, which enables more photons to pass through the top layer into the absorption layer, and thus increase the number of carriers generated, and the resulting power output.

The devices were fabricated in multiple reactors to reduce the possibility of cross-contamination of the dopant materials into the low-defect intrinsic layers.

Table 2.1: Summary of photovoltaic device layers shown in figure 2.3

Layer	Material	Method	Reason
n^+	n^+ a-Si:H	ECR-PECVD	Forms junction
i-3	a-Si:H	ECR-PECVD	Blocks P
i-2	a-Si:H	HW-ECR	EHP Gen.
i-1	a-(Si,C):H	ECR-PECVD	Blocks B, E_g matching
p^+	p+ a-SiC	ECR-PECVD	Forms junction
ITO	ITO	Sputtering	TCO contact

Table 2.1 shows a summary of the device layers shown in figure 2.3, including what deposition method was used to deposit the material. The buffer layers on either side of the i-2 layer deposited by HW-ECR help ensure both band-gap matching and efficient blocking of dopant migration into the HW-ECR layer during subsequent processing.

Cross-contamination is important to eliminate because it is detrimental to minority carrier transport in the device. Both carriers generated in photo-generation events must be captured to provide power to an outside circuit in an amorphous silicon photovoltaic device. If there was contamination of the intrinsic layer by phosphorus, many charged defect states would be formed creating very efficient hole traps. These hole traps would decrease the hole lifetime of the device, the range of the material, and thus degrade quantum efficiency. Figure 2.4 shows two electric-field intensity diagrams for sample i-layers. The diagram for the low-defect density material shows the solid unbiased field profile and the dashed forward-biased field profile both above 10^3 V/cm, which will still force the material to behave as field-limited. In the defective material to the right, notice that although the
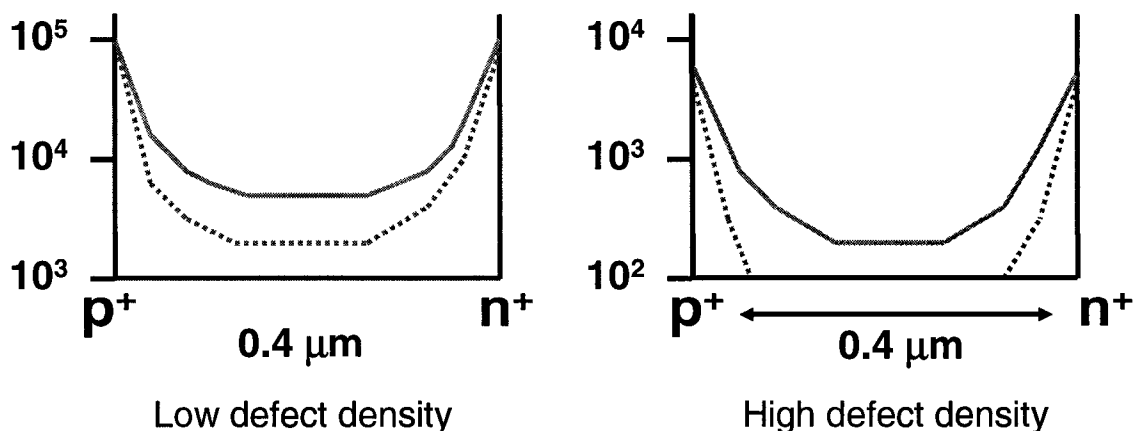

Figure 2.4: Electric field intensity diagrams for sample i-layers in p-i-n devices

unbiased solid line is above 10^2 V/cm, the forward biased dotted line goes to essentially zero field as there are enough charged defects to develop sufficient space-charge to compensate for the field. For the length that there is non-sufficient field, the devices exhibits diffusion-limited transport, and this is detrimental to the QE of the device as typical diffusion lengths are 1/3 of the i-layer thickness, so it is highly unlikely that carriers will cross the entire layer to be collected.

2.6: Contact Deposition

Several types of contacts were used in the fabrication of p-i-n devices, n-i-n devices, and the thin films for electrical characterization. Metallization was used to deposit the contacts for the thin films and the n-i-n devices for SCLC characterization, while reactive sputtering was used to deposit the transparent conductive contact made of indium tin oxide (ITO) used on the p-i-n solar cell devices.

2.6.1: Metallization

Electrical measurements were performed on thin films deposited on Corning 7059 glass and the n-i-n devices deposited on polished stainless steel. For electrical characterization of the thin films, coplanar contacts such as the ones shown in Fig. 2.5a were deposited onto the surface of the film. The n-i-n devices had chromium dot contacts deposited on their surfaces, much like the ones represented in Fig. 2.5b.

Both contact types were deposited in the same apparatus consisting of a glass bell jar evacuated by a large Leybold turbomolecular pump. Inside the bell-jar, chromium rods are resistively heated below a fixed plate with four holes for placing

the masked samples over. A shutter is placed below the fixed plate to control the length of metal deposition.

The metallization process begins by loading the sample with appropriate mask placed over the thin film surface. The bell-jar is then roughed out and then the gate valve is opened slowly to allow the turbo pump to evacuate the chamber to below 3×10^{-6} Torr. Once the desired base pressure is attained, the voltage across the chromium rods is gradually increased until the chamber pressure first increases, then decreases at 10 V, 15 V, then 18 V, and finally 23 V. At the final voltage setting, a piezoelectric crystal deposition controller is started and 100Å of chromium is pre-deposited with the shutter closed to remove the outer layer on the chrome rods that may be contaminated from atmospheric gases, and to bury those contaminants beneath a layer of chromium deposited on the interior surface of the deposition chamber. Immediately after the pre-deposition, the thickness monitor is again started at the same time as the shutter is opened, and 500Å of chromium is deposited. After deposition, the sample is removed from the bell-jar and silver paint
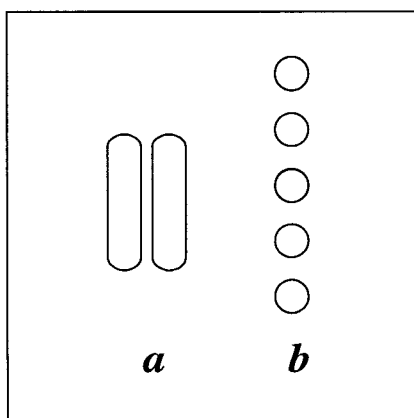
Figure 2.5: Diagram for mask of coplanar contacts (*a*) and chromium dot contacts (*b*)

is applied to prevent chrome oxidation. The sample is placed on a heated surface for 10-20 minutes to remove the solvent from the silver paint before being placed in an oven set to 160ºC oven for 1.5 hours prior to electrical testing.

2.6.2: Reactive Sputtering

The p-i-n devices are characterized using transparent conductive oxide contacts, much like commercial amorphous silicon solar cells use. The material deposited for these contacts is sputtered from an indium-tin oxide (ITO) target in an argon plasma with a small amount of oxygen introduced into the sputtering atmosphere. The substrate is heated to 175°C during the deposition and the deposition pressure is 5 mTorr. The flows of argon and 1% O_2 in argon balance are controlled by simple Matheson screw valve flow meters where flow is indicated by a weighted ball in a graduated glass tube.

The sputtering reactor consists of a large vacuum chamber evacuated by a Leybold turbomolecular pump. The pump can be closed off to the system by a gate valve, and the chamber itself has two sputtering targets and two Advanced Energy
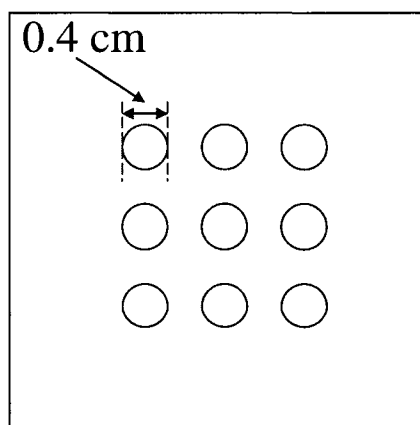

Figure 2.6: Device mask for depositing ITO contacts on solar cell devices

plasma guns to excite the argon atoms. The deposition time is controlled by a shutter, and generally occurs for 5 minutes, with a 2 minute period beforehand for the targets to clear off any surface contamination with the shutter closed. The gas flows during the deposition are 100% of the controller range for Ar and 20% for the 1% O_2 in Ar and the applied sputtering power is 20 W.

The ITO material is much more conductive than the amorphous semiconductors comprising the solar cell, but still less so than a metal contact. Average resistivities of ITO are ~2.6 x10$_{-4}$ Ω cm, and the optical transmittance in the visible spectra is generally from 80% to 90% [37]. These properties help maximize the amount of light absorbed and the amount of current available to power other devices.

The mask used for the ITO deposition is a thin nickel sheet with nine holes with a diameter of 0.4 cm each placed in them. The very thin mask eliminates shorts caused by thicker masks biting into the very thin device when tightened below the substrate holder that is placed into the sputtering chamber. Also, the thin mask allows for very minimal shadowing and therefore a more uniform and reproducible contact area. The mask is as shown in figure 2.6 above.

CHAPTER 3: CHARACTERIZATION METHODS

The materials and devices grown in this study were characterized by many methods. The data extracted is used as a basis of comparison between the hot-wire material and the materials subjected to ion bombardment. Of the methods used, some are specific to thin films of material grown on Corning 7059 glass, while others are used to characterize devices grown on stainless steel substrates, and still others are used on thin films deposited on silicon wafers. All of the characterization methods used in this study are described below.

3.1: UV/Vis/NIR Spectroscopy

An ultraviolet/visible/near-infrared (UV/Vis/NIR) spectrophotometer is used to determine the film thickness and the optical band gap from the absorption coefficient variations with photon energy. The system used to obtain the UV/Vis/NIR spectra is a split beam apparatus manufactured by Perkin-Elmer and interfaced to a standard PC.

Split-beam spectrophotometers generate a single monochromatic light beam that is then split by optics into two parallel beams of the same incident power. One of the two beams is aimed directly at photo-detector while the other passes through the sample and substrate. The difference in transmission is then measured at the photo-detector as the difference in the two beam powers.

The light not transmitted through the sample and collected is either reflected or absorbed. The substrate also reflects light, and as a result an interference pattern is observed in the transmission vs. wavelength spectra as shown in figure 3.1. The interference can be used to determine the thickness of the film by comparing the positions of adjacent peaks or valleys as in equation 3.1 [38]. In equation 3.1, n is
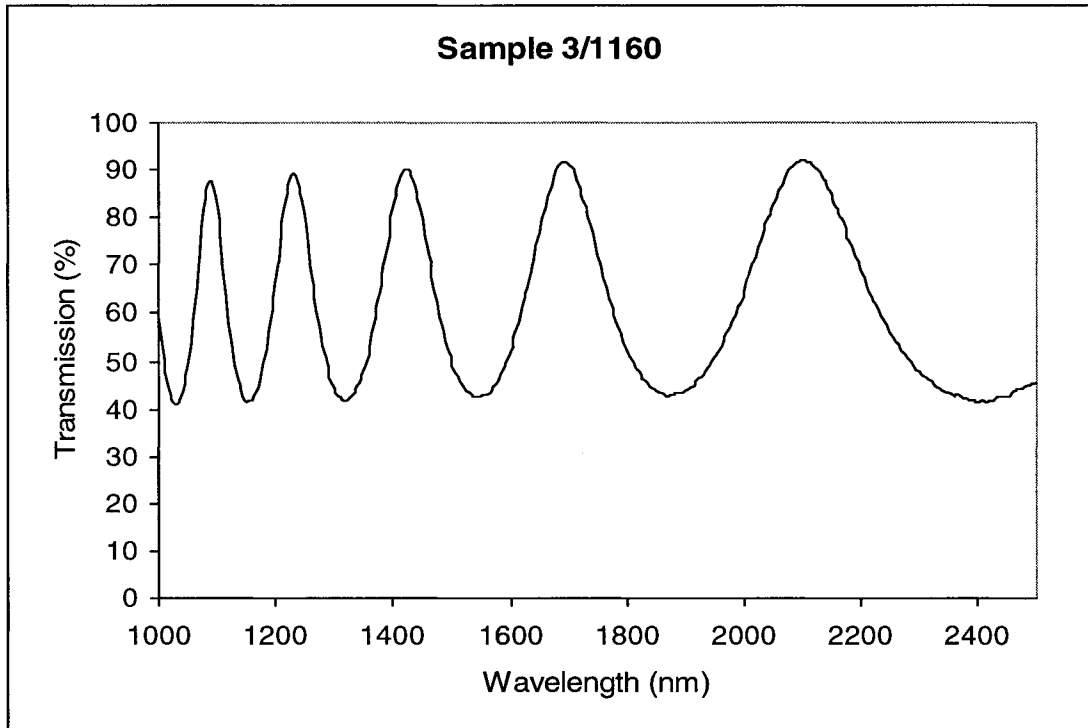
Sample 3/1160

Figure 3.1: Sample plot of spectrophotometer transmission data

the refractive index of the film between the two peaks, indicated by λ_1 and λ_2, and t is the calculated film thickness. This is the method used to calculate the thickness of

$$t = \frac{\lambda_1 \lambda_2}{2n(\lambda_1 - \lambda_2)} \qquad (3.1)$$

thin films deposited on 7059 Corning glass. For devices deposited on stainless steel substrates, the reflection assembly consisting of two mirrors that is inserted in the beam path and causes the beam to be incident upon the detector only when another mirror is placed atop the assembly. This technique generates a similar pattern as seen in figure 3.1, and equation 3.1 can still be used to obtain the total thickness.

In addition to the film thickness, the absorption coefficient can be obtained through UV/Vis/NIR. The absorbance vs. wavelength spectra can be measured using the spectrophotometer and by using index of refraction data from literature a reflection vs. wavelength spectra is generated based on equation 3.2, where n is index of refraction and R is reflectance, both of which are function of wavelength.

$$n(\lambda) = \frac{1 + \sqrt{R(\lambda)}}{1 - \sqrt{R(\lambda)}}$$
(3.2)

In some cases for silicon-germanium films, actual reflection spectra are used instead, as literature data is not as readily available for these alloys as for amorphous silicon. The absorption coefficient is then calculated using the film thickness and both absorption and reflection as functions of wavelength, as shown in equation 3.3 [38].

$$\alpha(\lambda) = \frac{2.303 \cdot A(\lambda) - \ln\left[\frac{1}{1 - R(\lambda)}\right]}{t}$$
(3.3)

Once the absorption coefficient is known for a range of wavelengths, the material's band gap can be estimated. The optical gap can be approximated as the energy where the absorption coefficient is equal to 10^4 cm^{-1}, known as the E_{04} energy. This is a simple method of estimating the band gap of the material as its determination is made graphically from a plot of the absorption coefficient α vs. photon energy, such as figure 3.2. Care must be taken however to account for the reflection interference seen at lower energy values, as the actual absorption spectra is the difference of the curve traced by the top of the peaks and the curve formed by the bottoms of troughs caused by interference.
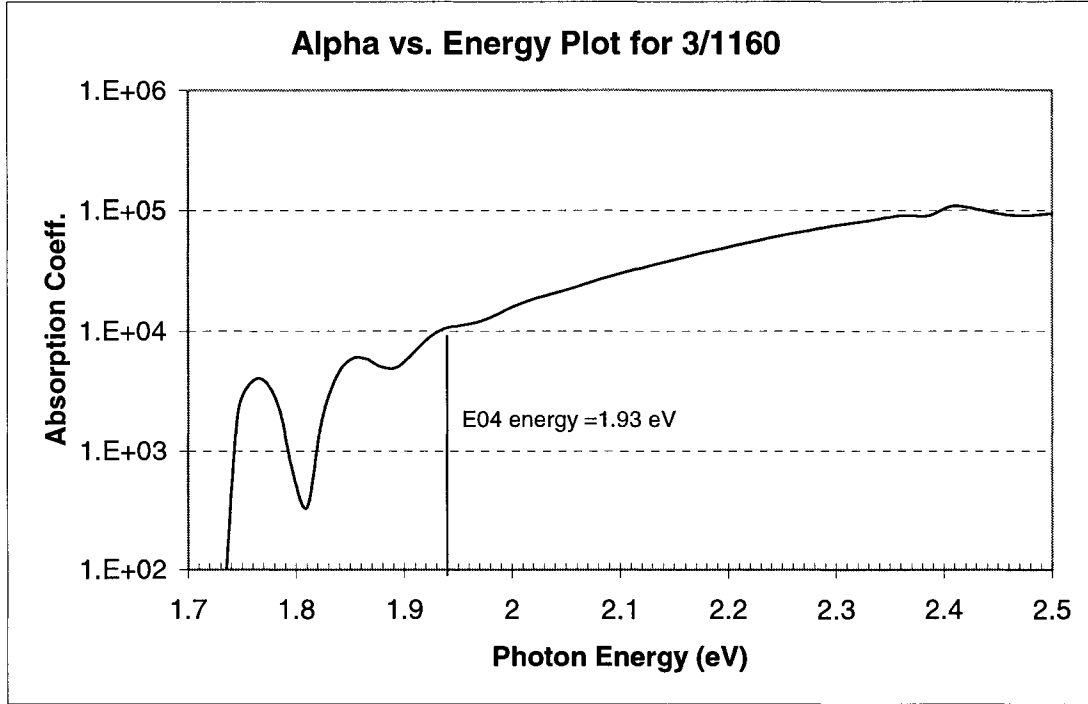
Figure 3.2: Sample plot of α vs. photon energy to determine the E04 energy

The band gap of the material can also estimated using Tauc's expression, shown in equation 3.4, which describes the absorption that occurs at photon energies above the E_{04} energy. The E_{Tauc} energy can be determined by plotting $(\alpha(\lambda) \cdot E_{ph})1/2$ vs. photon energy (E_{ph}), then finding the intercept of that line with the

$$\sqrt{\alpha(\lambda) \cdot E_{ph}} = B(E_{ph} - E_{Tauc})$$ (3.4)

x-axis. These two approximations for the material's band gap should agree such that E_{Tauc} is ~.15 eV less than E_{04} for hydrogenated amorphous silicon. A typical plot used for the determination of Tauc's Gap is shown in figure 3.3. Tauc's gap is a more ambiguous measure of band-gap experimentally as the slope of the linear

region is sometimes difficult to determine. Unfortunately, Tauc's gap is more thoroughly based on the theoretical mobility gap between the conduction and valence bands whereas E_{04} is a more empirical parameter. It is important to measure the band gap as deposition parameters change because it gives an indication to the degree of crystallinity of the material, the germanium content, and the amount of hydrogen incorporated into the film. The E_{04} energy is preferable for reporting bandgap data as it has much less experimental ambiguity, however literature is strewn with materials characterized using Tauc's gap, so it is calculated here for comparison purposes.
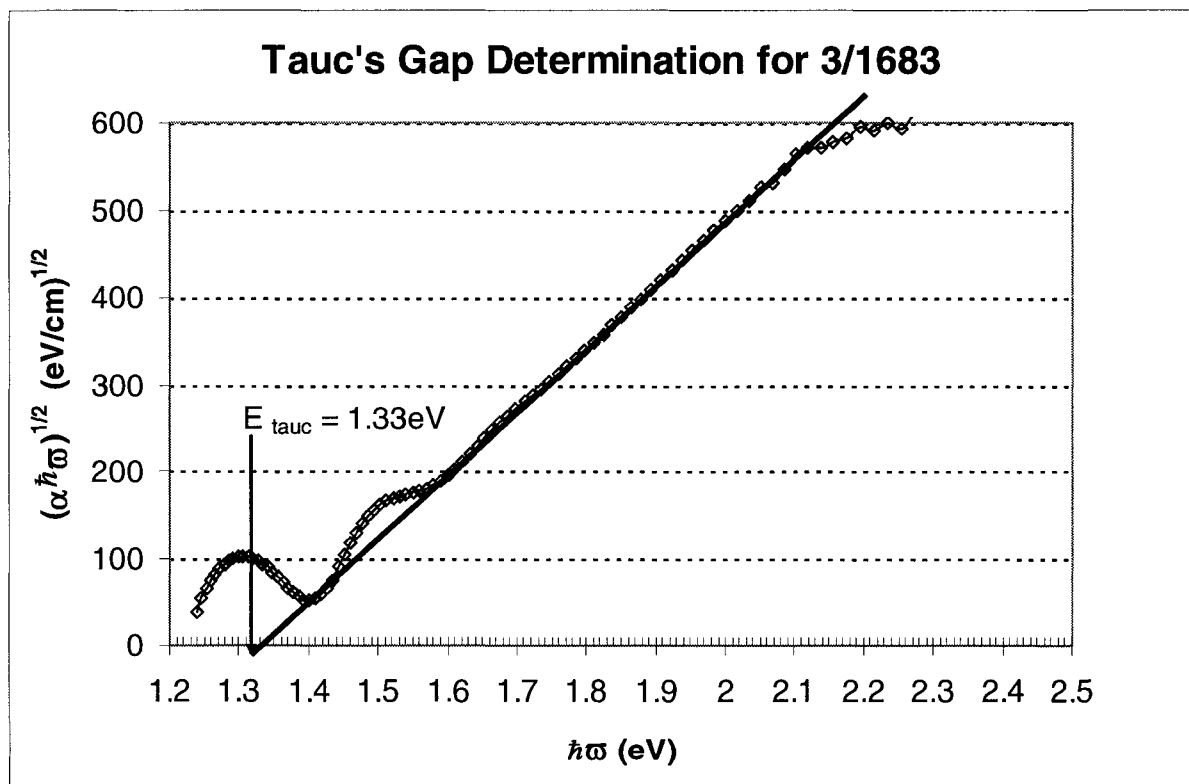

Figure 3.3: Sample plot for the determination of the Tauc's gap

3.2: Photo and Dark Conductivity Measurements

Determining the suitability of hydrogenated group IV alloy thin films for electronic applications begins by examining the conductivity of the material under illumination and comparing it to the material's conductivity under dark conditions. This comparison of conductivity is known as the photosensitivity of the material and is a general indication to the quality of the material as high quality a-Si:H has a photosensitivity greater than 10^5, a-(Si,Ge):H with an E04 gap of 1.5 ev is $\sim 10^2$, and crystalline silicon or germanium should be ~ 1. A large increase in the absolute conductivity of the material should be seen as crystalline nature of the material varies from amorphous to single crystal material as the mobility and lifetimes of the crystalline material are much greater than the amorphous material.

The light and dark conductivity measurements are performed in an apparatus consisting of a large aluminum heat sink cooled by a fan placed in a light impervious box. Two spring-loaded probes are then placed on the co-planar metallic contacts described in the contact deposition section. These probes are connected to a Keithly 617 electrometer and a Keithly 230 voltage source to supply a 100V bias between the two coplanar contacts and measure the small resulting current. Steel panels and an aluminum door sealed with Velcro and magnets enclose the sample and heat sink to form the light-tight box that prevents light from striking the during the dark conductivity measurement. The photo current is measured by turning on a quartz lamp directly above the sample that has a calibrated aperture between itself and sample so that 100 mW/cm^2 is incident upon the sample, which is the standard AM 1.5 illumination that is reported in literature for photoconductivity.

The conductivity is calculated as shown in equation 3.4 by multiplying the width between the coplanar contacts (W) with the current measured (I) during the

$$\sigma_{L,D} = \frac{WI}{LVt} \qquad\qquad (3.4)$$

test. This product is then divided by the product of the contact length, applied voltage, and the film thickness. For these experiments, the ratio of L/W was 20.

3.3: Infrared Spectroscopy and Hydrogen Content

Another method used to describe the quality of a-(Si,Ge):H thin films is IR spectroscopy. The infrared spectrum of hydrogenated amorphous silicon can be used to determine the hydrogen content of the film and the microstructure parameter R [39]. The hydrogen content of amorphous silicon-germanium alloys is an important parameter because excess hydrogen reduces the conductivity of the material and is associated with Stabelar-Wronski degradation. [40] The microstructure parameter R, as defined in equation 3.6 [39] for silicon bonds and equation 3.7 for germanium bonds indicates the relative amount of dihydride bonding in the material that is strongly associated with S-W degradation and generally decreased electronic properties.

$$R_{Si} = \frac{A_{SiH_2}}{A_{SiH} + A_{SiH_2}} \qquad\qquad (3.6)$$

$$R_{Ge} = \frac{A_{GeH_2}}{A_{GeH} + A_{GeH_2}} \qquad\qquad (3.7)$$

Infrared spectroscopy requires deposition of the subject material on a silicon wafer that has had both sides polished to avoid scattering problems. After the material is deposited, it is placed in the IR spectrometer with a background sample of wafer. The spectrometer then measures the mid-IR spectral absorbance of the

background and sample at a 4 nm resolution from 4000 cm^{-1} to 400 cm^{-1} (2500 nm to 25000 nm) and produces a smoothed curve as shown in Fig. 3.4.

To determine the hydrogen content of the film, the region of the spectra from 500c cm^{-1} to 800 cm^{-1} is examined, and a Gaussian peak fitted to the 640 cm^{-1} peak and the 565 cm^{-1}peak. The area of the relative absorbance peak at 640 cm^{-1}, which is due to SiH, SiH$_2$, and SiH$_3$ wagging modes, or the 565 cm^{-1} peak which is analogous but due to germanium, is then multiplied by a conversion factor to determine the atomic hydrogen percent of the material, as shown in equation 3.8
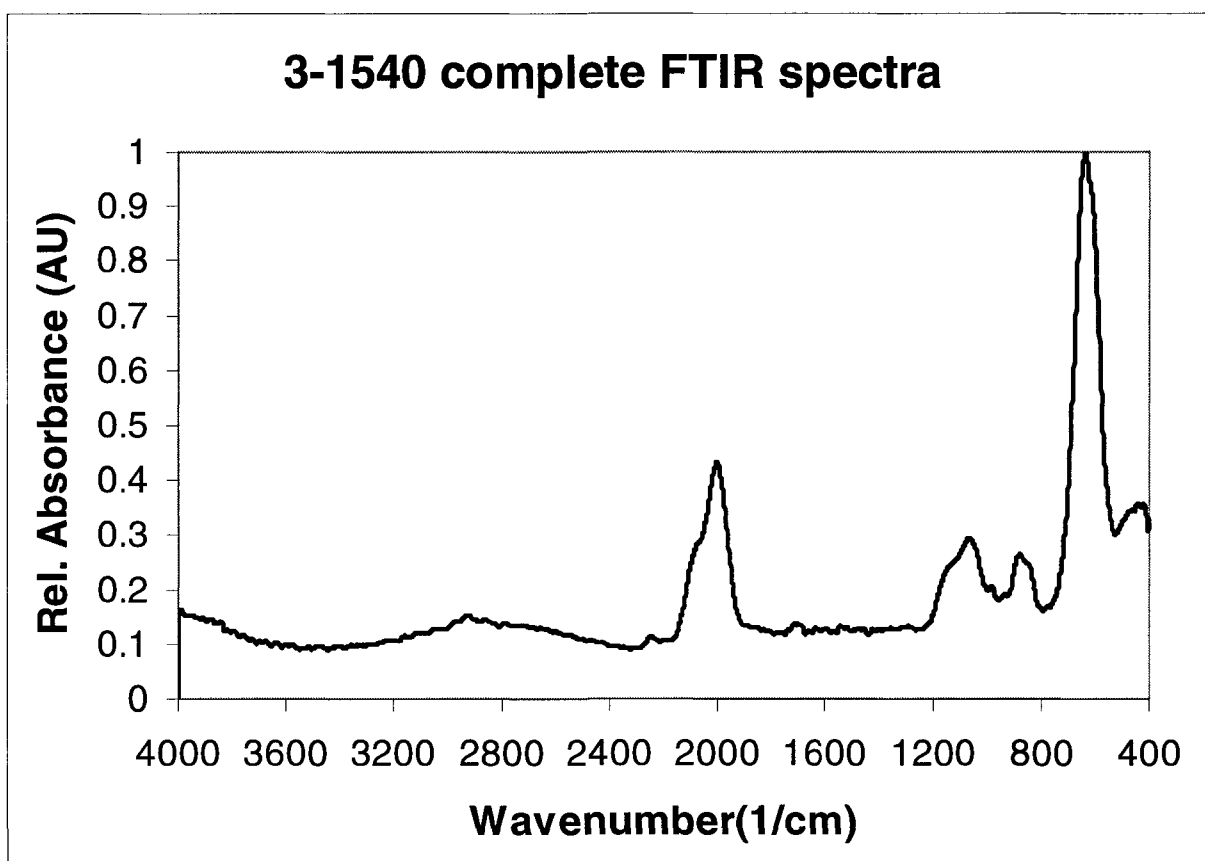

Figure 3.4: FTIR spectra of a-Si:H deposited by HWCVD

[41], where C_H is the hydrogen fraction in atomic percent, A_{640} is the area of the relative absorbance peak at 640 cm^{-1}, and t is the film thickness.

$$C_H = 1.125 \cdot \frac{A_{640}}{t}$$ (3.8)

The silicon microstructure parameter R_{Si} is calculated from equation 3.6, however the peaks for the SiH$_2$ and SiH stretching at 2090 and 2000 cm^{-1}, respectively need to be deconvoluted into separate Gaussians. The same is true for the R_{Ge} parameter where the GeH peak at 1880 cm^{-1} and the GeH$_2$ peak at 1970 cm^{-1} needs to be modeled as independent Gaussian curves whose sums create the overall spectra shape. In addition, the baseline is corrected to remove effects from
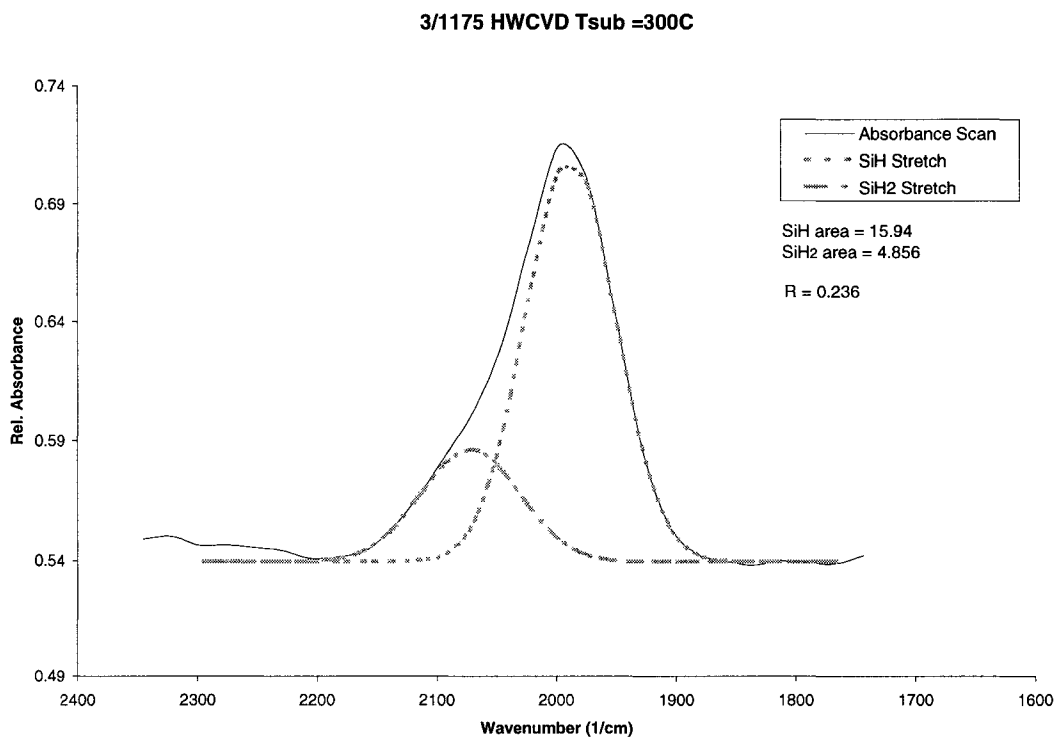

Figure 3.5: Sample spectral deconvolution for microstructure parameter determination

the thin film reflection interference. All of these functions are performed in Origin, a mathematical software package that can easily model Gaussians to fit the shape of the spectra. The baseline is modeled as a polynomial where specific points are chosen on the spectra that are known to be the baseline and the remainder of the function is modeled. Figure 3.5 shows an example of a de-convoluted spectrum used to quantify the peak areas for SiH and SiH_2 peaks in a hydrogenated amorphous silicon sample and give 95% confidence limits that were used to calculate the error limits to the measurement.

3.4: Activation Energy

The conductivity of a semiconductor is proportional to the number of carriers available to transport charge from one reservoir to another, such as from one ohmic contact to another located some distance away. Since the intrinsic concentration of carriers is dependent upon temperature, as is the number of ionized impurities in a doped material, current should vary with the material temperature according to an Arrhenius relationship. Using the definition of conductivity and the drift equation, it is easy to relate the current of a semiconductor under steady bias to temperature though equation 3.9, where E_A is activation energy, k_B is Boltzman's constant, T is the temperature in Kelvin, and I_0 the baseline current, or pre-exponential factor.

$$I = I_0 e^{-\frac{E_A}{k_B T}} \tag{3.9}$$

For amorphous, lightly doped semiconductors, the vast majority of electrons will be located in states at or below the Fermi energy and since it is these carriers that need to be energized into the conduction band for current to flow, E_A is a measure of the location of the Fermi energy in these materials.

When measuring this parameter, the sample is placed on a heated aluminum block and a spring-loaded contact is placed on each side of the coplanar contacts described earlier. The sample is then sealed in a light impervious box and heated to ~ 210°C and then a 100V bias applies. Current measurements are taken from 210°C to 130°C in 10 degree increments and then $\ln(I/I_0)$ is plotted vs. 1/T. This plot is then modeled by linear regression and the slope of that line multiplied by k_B to determine the activation energy. High quality a-Si:H materials typically exhibit activation energies approximately 0.9 eV, while a-(Si,Ge):H materials exhibit activation energies of approximately one-half their E_{04} bandgap.

3.5: Sub-Band Gap Absorption

As the name implies, the sub-gap absorption measurement in amorphous semiconductors evaluates the absorption of low energy photons whose energy is below that of the optical gap of the semiconductor. This measurement relies on the dual-beam photoconductivity technique developed by Wronski et. al. [42], where a strong DC beam is used to fix the quasi-Fermi levels of the material, keeping available states in the mid-gap region filled with photo-generated carriers. The second beam is an AC beam fixed at 13.5 Hz by a chopper to remove noise associated with the 60 Hz current used to power the equipment. The beam from the light source is then modified by diffraction grating in a monochrometer to produce a narrow wavelength spectrum that is then aimed at the film between the coplanar contacts to supply additional carriers and increase the material's conductivity. The AC beam, after passing through the monochrometer and chopper, passes through a series of high pass filters to reduce the harmonic frequencies associated with the beam exiting the monochrometer, and to prevent low-wavelength light from reaching the sample until it is desired. The wavelengths used for typical a-Si:H
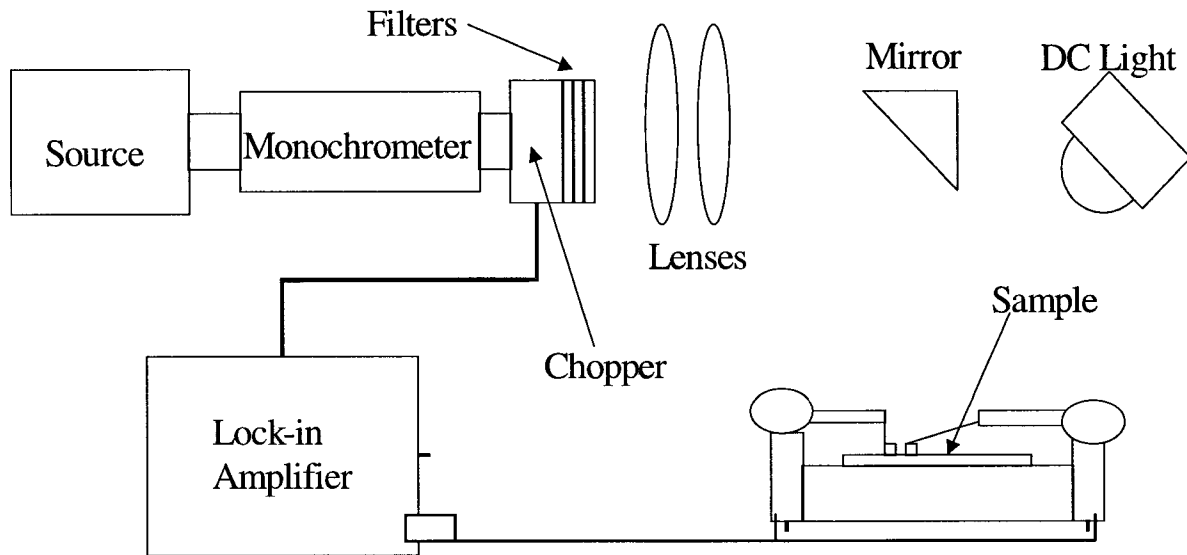
Figure 3.6: Dual-beam photoconductivity apparatus used for sub-band gap absorption

characterization varies from 1200 nm to 600 nm, and filters with roll-off frequencies of 700 nm, 900 nm, and 1200 nm are used. For the E_{04} = 1.5 eV a-(Si,Ge):H, typical measurements were from the range of 1500 nm to 740 nm, using the same filters as the a-Si:H. A schematic of the device used in the dual-beam photoconductivity technique is shown as Fig. 3.6.

In addition to the generation, diffraction, and filtering to the AC light beam, it is collimated through lenses and focused onto the sample by a mirror. The care taken to ensure the quality of this AC beam is critical, as the additional current generated by it is measured with a lock-in amplifier to determine the absorption coefficient as a function of photon wavelength. From this absorption coefficient data, another parameter known as the Urbach energy (E_{OV}) can be determined, as shown in equation 3.10, where E_g is the band-gap, h is Planck's constant and v the wavelength.

The E_{OV} value of a sample is an important characterization parameter as it has been shown to be a function of the material's defect density [43]. The Urbach energy is used as an indication of material quality, as values less than or equal to 47 meV result only from higher quality films.

$$\alpha = \alpha_0 e^{-\frac{E_g - h\upsilon}{E_{OV}}} \qquad (3.10)$$

3.6: Space Charge Limited Current Defect Measurement

Another method for estimating the defect density of hydrogenated amorphous materials is the space-charge-limited current method described by den Boer [44]. In this method, a n+-i-n+ device is used, where the n+-layers were fabricated using rf-glow discharge and the i-layer by HWCVD or ECR-HW CVD. The n^+ layers are of great importance, and for a-(Si,Ge):H materials, the top n^+ layers must be an alloy of silicon and germanium, or a non-symmetrical curve results, and the data is called into question. The asymmetry of the curve is caused by charge trapping at the top interface. The devices had the chromium dot contacts deposited on the film surface to define the device area and were deposited on stainless steel. The devices were then placed on a heated surface and placed in a light-tight box where they were subject to a bias voltage through the device. This voltage was then varied over the range from 0 V to the E_{04} band gap energy in 0.1 V increments. At each voltage point, the current flowing through the device is measured, and then the data is used to calculate the trap density of states as a function of energy, as shown in equation

$$N_t(E) \approx \frac{2\varepsilon_s \Delta V}{qt^2 \Delta E_f} \qquad (3.11)$$

3.11, where N_t is the trap density, ΔV is the voltage differential between two measured points, t the i-layer thickness, and q the charge of one electron. The parameter ΔEF is defied in equation 3.12, where k_B is Boltzman's constant, and J_x and V_x are the current and

$$\Delta E_f = k_B T \cdot \ln\left(\frac{J_2 V_1}{J_1 V_2}\right)$$

(3.12)

voltage of a measured point, respectively. By applying the data to these two equations, it is possible to determine the trap density at the Fermi energy, where defect states can greatly decrease the transport characteristics of the material. In general, materials with a lower SCLC defect density are better suited for photovoltaic applications.

3.7: Current-Voltage Characterization

The current-voltage characterization of a p-i-n solar cell is very important as it describes the behavior of the diode that is formed by the deposited layers. The J-V curve can also tell us much about the efficiency of the solar cell, whether it be the maximum power provided, the absorption efficiency noted from the short circuit current, or the material dependent open circuit voltage.

3.7.1: Short Circuit Current Density

The short circuit current is an indication of the transport properties and absorption efficiency of the intrinsic absorption layer. To fully understand the short circuit current, it is necessary to understand both the physical structure of the devices, and its circuit-element model, as shown in figure 3.7. The short circuit current density (J_{sc}) is the current that flows between the device terminals under
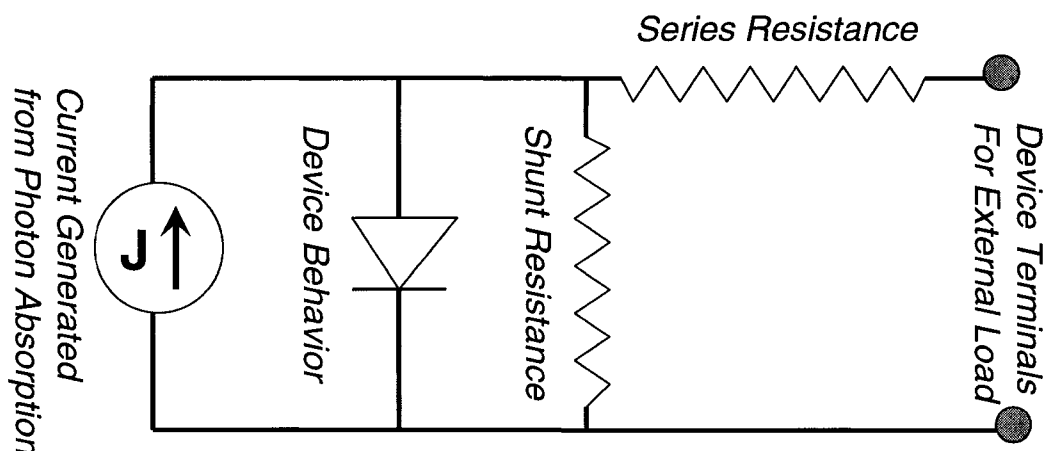
Figure 3.7: Equivalent circuit model for a p-i-n solar cell device

illumination with zero bias and with a load resistance near zero. The short circuit current is then a measure of the current generation of the cell for a given incident photon spectrum. Therefore to maximize J_{sc}, it is necessary to use an i-layer that has an absorption spectrum to match the light available to power the device. This relation ship is shown in equation 3.13, where $N_{ph}(E)$ is the spectral photon energy distribution and $G(E)$ is the number of electron-hole pairs collected by the device for each photon energy. In addition, the effects of the optical engineering of the device are accounted for, such as the photon absorption in the contacts and the reflection of photons at the device surface. These effects are represented by the $(1-e^{-\alpha c(E)tc})$ and $(1-R)$ terms, respectively, as $\alpha_c(E)$ is the absorption coefficient of the contact material and R is the reflection coefficient.

$$Jsc = q \int (1-R)(1-e^{-\alpha_c(E)t_c})N_{ph}(E)G(E) \cdot dE \qquad (3.13)$$

$$V_{oc} \approx \frac{kT}{q}\left[\ln(J_{sc}) - \ln\left(\frac{qW_d}{2\tau}\sqrt{N_cN_v}\right)\right] + \frac{E_g}{2q}$$ (3.17)

3.7.3: Fill Factor

The fill factor is a measure of the power conversion efficiency of the photovoltaic cell that depends upon the maximum power output of the cell and the product of V_{oc} and J_{sc}, as shown in equation 3.18. To obtain good fill factors, the

Typical J-V Curve for a-Si:H device
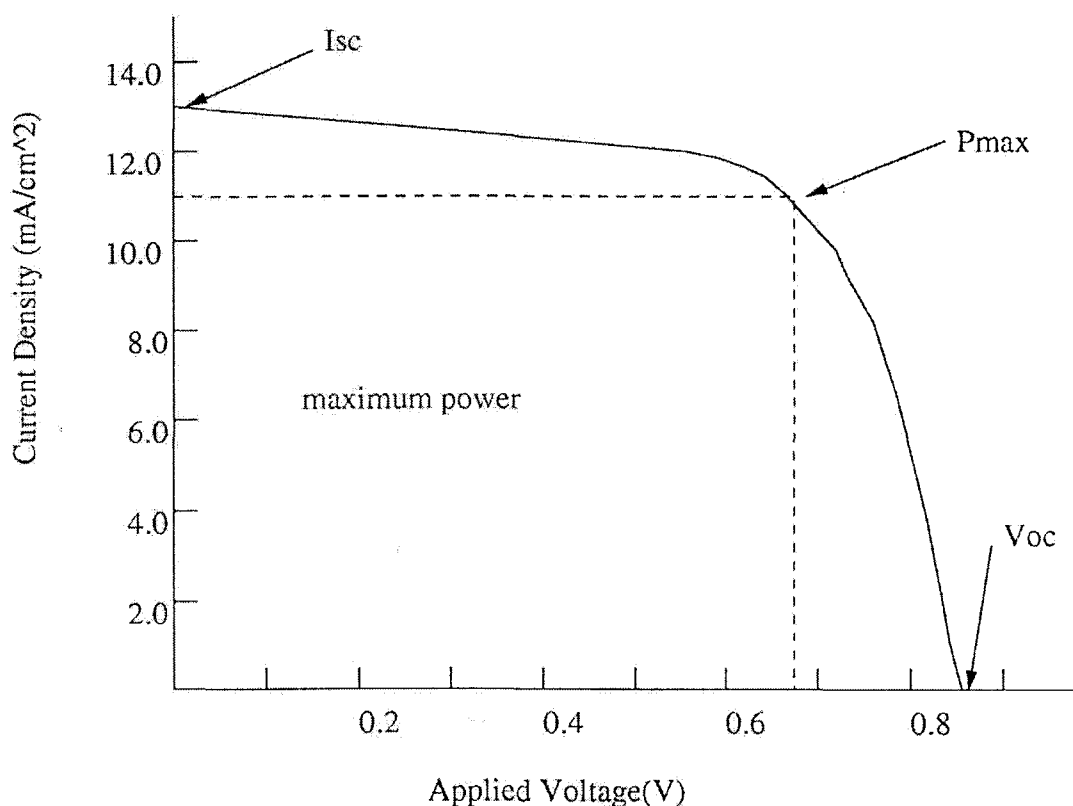
Figure 3.8: Sample J-V curve for illuminated a-Si:H photovoltaic device [45]

diode curve must be similar to the one shown in figure 3.8, where the edges are sharp and the curve itself is rather square. Well designed, high-quality devices composed of a-Si:H have V_{oc} of ~0.85V and fill factors close to 70%. In contrast, devices containing 1.5eV a-(Si,Ge):H generally have fill factors approaching 65% with lower V_{oc}.

$$ff = \frac{P_{max}}{V_{oc} \cdot I_{sc}}$$ (3.18)

The fill factor itself requires that the device be capable of efficiently converting the photons incident on its surface into collected carriers. Therefore the device must have good interfaces free from traps, outstanding material properties in the i-layer, as well as ohmic contacts on the top and bottom surfaces. In terms of the circuit model of figure 3.7, a high fill factor requires low series resistance and very high shunt resistance along with good current generation.

3.8: Quantum Efficiency

The quantum efficiency of a solar cell describes the absorption behavior of the cell and provides insight to the overall performance of the device. The quantum

$$QE = \frac{1}{1-\alpha^{-2}L_n^{-2}} \left\{ 1 - \frac{1}{\alpha L_n} \cdot \frac{\frac{SL_n}{D_n}(\cosh(t/L_n) - e^{-\alpha t}) + \sinh(t/L_n) + \alpha L_n \cdot e^{-\alpha t}}{\frac{SL_n}{D_n}\sinh(t/L_n) + \cosh(t/L_n)} \right\}$$ (3.19)

$$QE = \frac{\alpha L_n}{1 + \alpha L_n}$$ (3.20)

efficiency of a solar cell is the ratio of absorbed photons to collected carriers. Equation 3.19 describes in detail the quantum efficiency of the solar cell, taking into account the surface recombination velocity S and the initial concentration of carriers at the illuminated surface n_{po}. However for most cases when the diffusion length L_n is much less than the film thickness t, this equation can be simplified into the form seen as equation 3.20. In both cases however, the absorption coefficient and quantum efficiency are functions of photon energy.

The QE spectrum, as shown in figure 3.9 can indicate problems with the device design. For example, if the QE is less than ~80% at its peak value, then the device thickness is too large for the material that composes the i-layer. The carriers
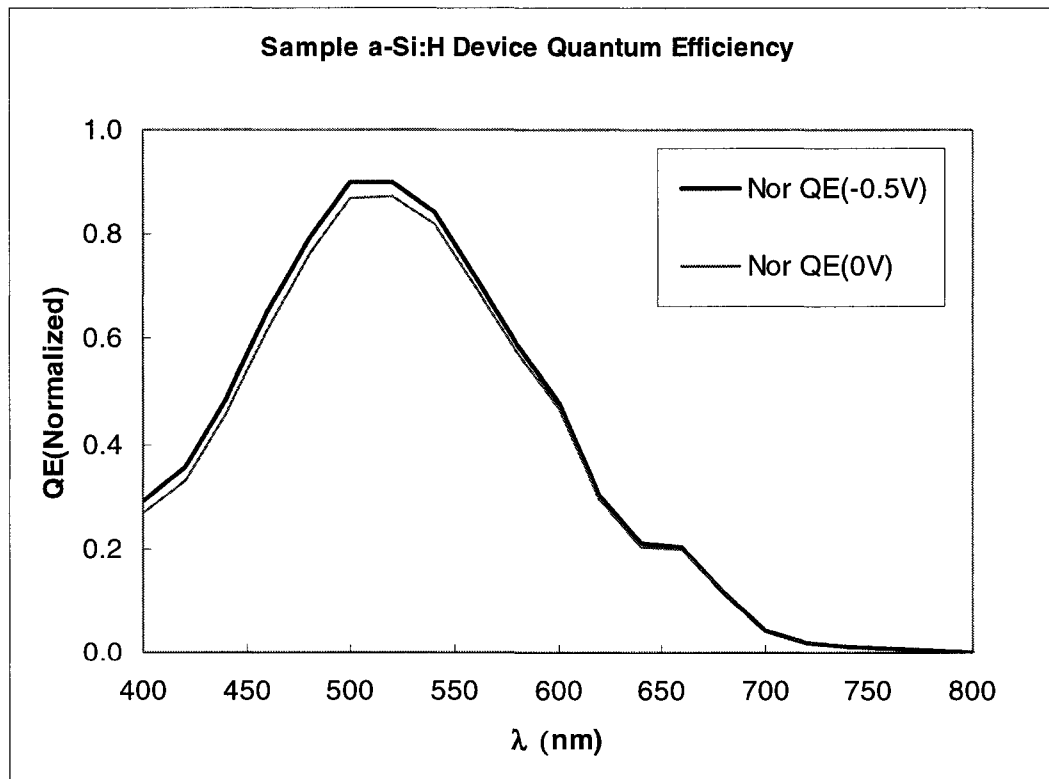
Figure 3.9: Sample QE of a PECVD a-Si:H device with ITO contacts

are recombining before making it to the n^+ or p^+ regions and therefore not being collected. The device therefore needs to have a higher induced electric field across the i-layer, so a doping profile or band-gap grading may be necessary. Also important is the location of the QE maximum. This is a function of the material of the device, and needs to be matched to the peak of the spectrum of light available for energy conversion.

The QE measurement itself is performed using the dual beam photo-conductivity apparatus described in section 3.5 and shown in figure 3.6. A measurement is taken at a small forward bias to understand how well the internal electric field of the devices is collecting the carriers, as the forward bias will reduce the field somewhat. Another measurement is taken with no bias across the cell to observe the maximum absorption peaks and to observe the high energy photon absorption to deduce the quality of the p-i interface. The ratio of these two measurements is taken and should ideally be one, as for that case the internal electric field and material and interface quality is so good that the field reduction doesn't affect the transport of carriers; however, in practice an increase in this ratio is seen at low wavelengths.

CHAPTER 4: RESULTS AND DISCUSSION

The data stemming from this research will be presented in four distinct sections. The first section will show that the Hot-Wire ECR can produce better material than hot wire alone at a multitude of band-gaps. The second section will discuss the effect of plasma power and plasma ions generated on the a-(Si,Ge):H materials. A third section will review the results of varying the hot wire filament temperature while all other parameters are held constant. The fourth section of this chapter will focus on the results from fabricating the first ever photovoltaic devices using the HW-ECR process.

4.1: Comparison of Hot-Wire and HW-ECR Materials

Throughout this research, comparisons have been made between the materials deposited under ion bombardment conditions and those deposited in a plasma-free environment. Several different band-gaps were studied by combining silane and germane in different ratios as they flowed through the reactor. Care was taken in the study to ensure that aside from the presence of ions in the remote plasma chamber, nothing else was different. That is, when comparisons are made between a sample grown by HW-ECR using a 100W helium plasma and its analogue deposited by HWCVD, the HWCVD film was grown with inert helium dilution to ensure that the partial gas pressures were essentially the same.

In this study, four distinct Tauc energy band-gaps were studied: 1.75eV, 1.65eV, 1.55eV, and 1.45eV. These materials range from 100% Si (1.75eV) to approximately a 50% mix of Si and Ge (1.45 eV). Tauc gaps will be reported in this study to be consistent with literature; however E04 values are generally less ambiguous to measure.

4.1.1: $E_{Tauc} = 1.75eV$ material

The 1.75eV material is the easiest material to produce with high quality. This material has a higher tolerance for process variation, as there is no alloying with germanium occurring with this material. This material showed very high photosensitivity and photoconductivity values when deposited either by HWCVD or HWECR. Table 4.1 shows a direct comparison of three materials, one grown by hot-wire alone, one with the addition of ion bombardment, and the third by hot-wire alone at a higher substrate temperature. Note that the material grown with ion bombardment attains similar values for the reported metrics as the high temperature HWCVD film. This indicates that ion bombardment has a similar effect as increased substrate temperature does, in that it aids in hydrogen removal and in increasing silyl surface mobility [9]. The HW-ECR films and HWCVD films grown at higher temperatures have physical and electronic properties that are similar to reported high quality a-Si:H. Substrate temperature proves to be important when depositing high-quality a-Si:H at high growth rate, as shown in figures 4.1 and 4.2. In figure

Table 4.1: Comparison of best E_{Tauc} =1.75eV materials grown by HWCVD and HWECR [9]

MATERIAL	HWCVD 250°C	HW-ECR 250°C	HWCVD 300°C
σ_{Photo} (S/cm)	9.0×10^{-6}	1.2×10^{-4}	1.2×10^{-4}
$\sigma_{Photo}/\sigma_{Dark}$ Ratio	2.7×10^{4}	1.1×10^{5}	4.2×10^{5}
E_{ov} (meV)	64	46	45
α(1.2eV) (cm^{-1})	15	1.0	0.7
Microstructure R_{si}	0.23	0.11	0.15
SCLC def. (cm^3-eV)	5.0×10^{16}	1.0×10^{16}	1.0×10^{16}

4.1, the Urbach energy of the samples is shown as a function of substrate temperature. Notice that at the highest substrate temperatures, an optimal E_{ov} is seen at approximately 45 meV for both deposition types. This occurs because the hydrogen abstraction and surface mobility of of the adding silyl radicals is no longer thermally limited. At lower temperatures where the there is not enough thermal energy to efficiently add new silyl radicals, the ions add the needed energy to create a more ordered system that results in better E_{ov} values. Figure 4.2 shows the microstructure of a-Si:H as a function of substrate temperature, and again we see

a-Si:H Urbach Energy vs. Temperature at 105 mTorr-cm
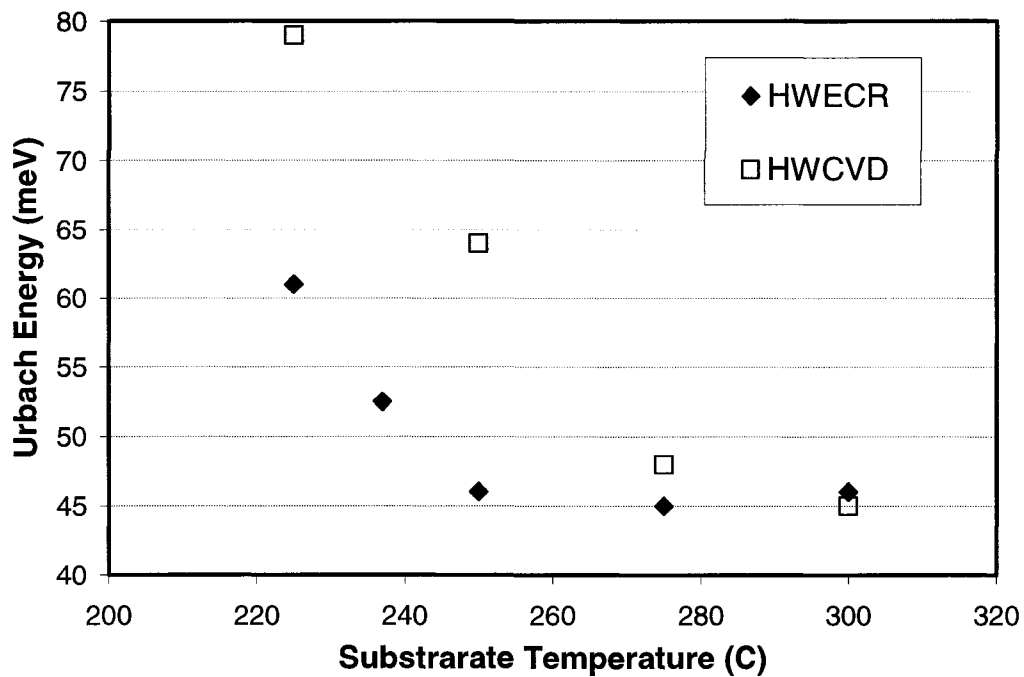
Figure 4.1: Urbach energy values for a-Si:H that exhibit a trend for decreasing E_{ov} with increased substrate temperatures [46]

**Microstructure Fraction R vs. Substrate
Temperature**
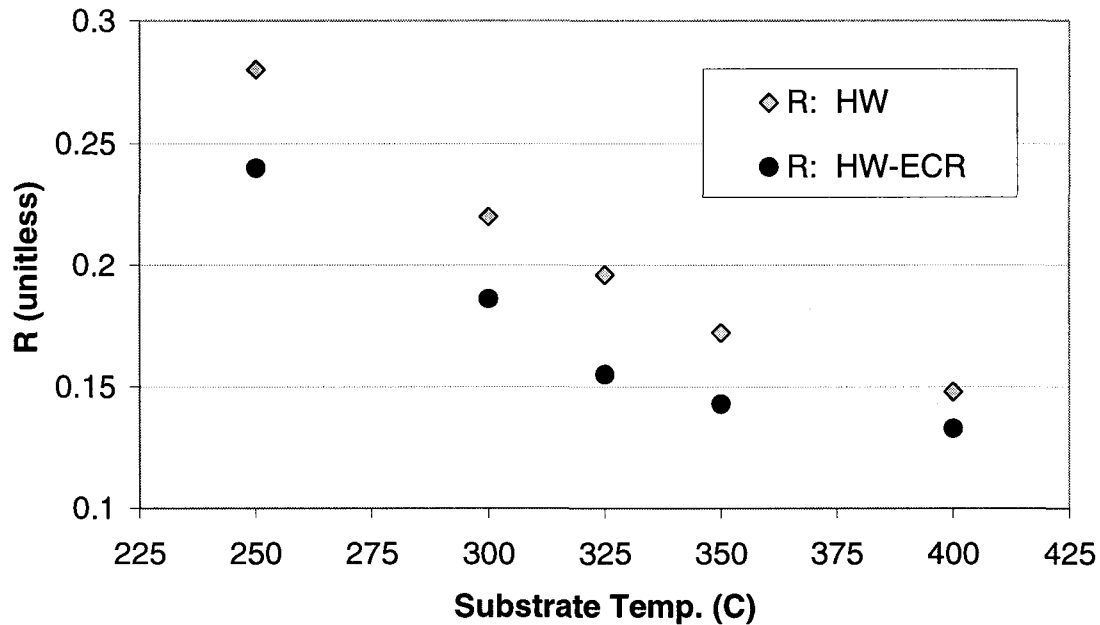
Figure 4.2: a-Si:H microstructure (R) as a function of substrate temperature indicating

improvement of R with ion bombardment [46]

that the ions produce a reduced microstructure [35,46], indicating a more ordered
system, until higher substrate temperatures are used.

4.1.2: $E_{Tauc} = 1.65eV$ material

The 1.65eV material has a slight amount of germanium added to the reactive
gasses to introduce enough Ge into the amorphous matrix to decrease the bandgap
slightly. This material deposits almost as quickly as the 1.75eV material, however
there is hydrogen dilution built into the reaction chemistry due to the germane being
a 10% mixture with hydrogen gas. The hydrogen dilution is for safety in handling the

compressed germanium cylinders, and was therefore not changed during the course of the research.

Table 4.2 shows a comparison of HWCVD and HW-ECR material having Tauc's gaps of 1.65 eV that were deposited at identical substrate temperatures, 10 mTorr chamber pressures, helium dilutions, and 2200°C filament temperatures.

Table 4.2: Comparison of E_{Tauc} = 1.65eV materials grown by HWCVD and HWECR

MATERIAL	HWCVD 250°C	HW-ECR 250°C
σ_{Photo} (S/cm)	3.0×10^{-7}	1.5×10^{-6}
$\sigma_{Photo}/\sigma_{Dark}$ Ratio	1.1×10^{3}	1.1×10^{5}
E_{ov} (meV)	63	46
α(1.2eV) (cm^{-1})	50	7
Microstructure R_{si}	.25	.24
Microstructure R_{Ge}	.11	.02

Notice that these materials have large differences in their photo-conductivities, Urbach energies, and microstructure ratios. Again, this is due to the temperature limitation of the HWCVD material. If the deposition temperature was increased, undoubtedly an improvement in the material would ensue, just like the a-Si:H data, especially since there is a relatively low amount of germanium incorporated into this material.

The material grown without ion bombardment is much more defective than its analogue grown with the assistance of ions. This can be deduced from the sub band-gap absorption curves shown in figure 4.3, and is indicated by the Urbach energy values. The sub band-gap absorption spectra is determined by the disorder

Sub Bandgap Absorption Coefficient for ETauc =1.65 eV a-(Si,Ge):H
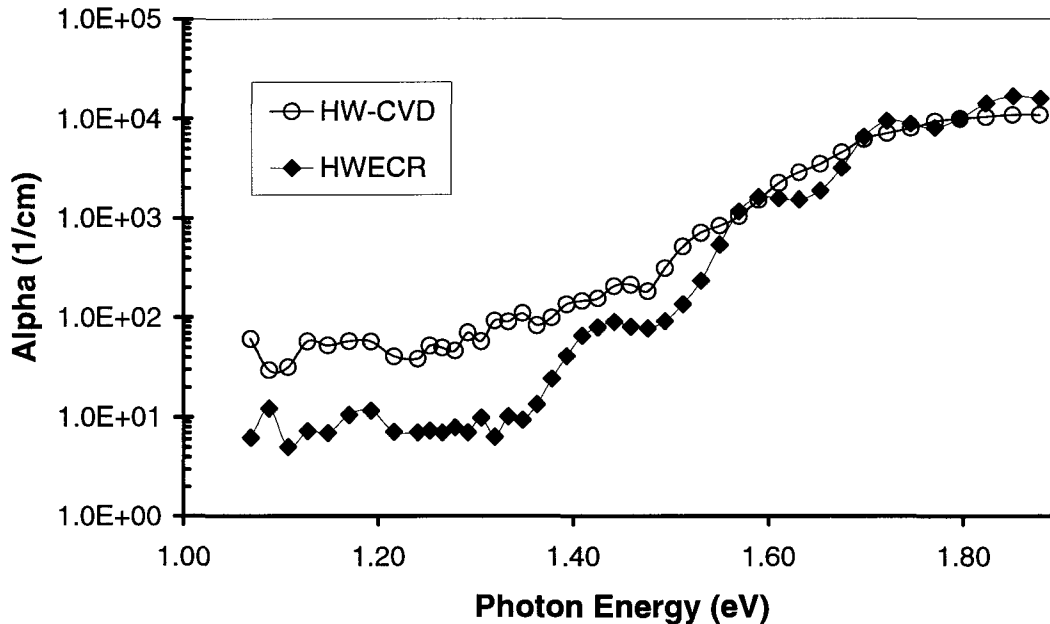
Figure 4.3: Sub band-gap absorption spectra comparison for a-(Si,Ge):H grown using different methods but with the same PD and substrate temperature

of the material, that is, absorption occurs when there is an allowable transition from one state to another. If the material is perfectly crystalline, then on would see essentially zero absorption between the band gap. In the amorphous material, however, there is inherent disorder in the bond lengths and strains, making a continuum of states between the band edges. When there is more disorder in the system there are more defect states to act as traps for carriers, and the absorption coefficient of the material will be higher. In figure 4.3 when comparing the HWCVD film to the HW-ECR material, one sees a drastic increase in the mid-gap absorption, and thus mid-gap defect states, along with a great increase in the tail-states that

compose the shoulder of the curve. In the HWCVD material, the shoulder is much broader, thus there are many more defect states in that material, and it is less suited for photovoltaic application.

4.1.3: E_{Tauc} = 1.55eV material

The 1.55eV material contains much more germanium than the 1.65eV material, and is therefore more difficult to deposit with high quality characteristics. Table 4.3 shows a comparison of two 1.55eV films that were grown at identical pressures, and substrate temperatures, varying only in the presence of ions. The material grown with hydrogen ion bombardment is outstanding, with very low Urbach energy and high photo-conductivity values for that band-gap. In Table 4.4, a comparison is shown between two materials grown using HWCVD only, however one had additional hydrogen dilution. This set of films shows how the penetrating property of the hydrogen radicals and the tuning of the gas phase reactions aids in the removal of excess hydrogen. The hydrogen dilution added to the material, in combination with the aided in creating a more ordered structure as deposition

Table 4.3: Comparison of E_{Tauc} = 1.55eV materials grown by HWCVD and HWECR

MATERIAL	HWCVD (H dil.)	H+ ion HW-ECR
σ_{Photo} (S/cm)	5.2×10^{-7}	2.8×10^{-6}
$\sigma_{Photo}/\sigma_{Dark}$ Ratio	9.7×10^{3}	6.6×10^{4}
E_{ov} (meV)	51	44
$\alpha(1.2eV)$ (cm^{-1})	20	.8
Microstructure R_{si}	.45	.17
Microstructure R_{Ge}	.21	0

Table 4.4: Comparison of E_{Tauc} = 1.55eV materials grown by HWCVD with and without hydrogen dilution

MATERIAL	HWCVD	HWCVD -low T_{fil}
σ_{Photo} (S/cm)	2.6×10^{-7}	5.2×10^{-7}
$\sigma_{Photo}/\sigma_{Dark}$ Ratio	4.2×10^{2}	9.7×10^{3}
E_{ov} (meV)	81	51
α(1.1eV) (cm^{-1})	200	20
Microstructure R_{si}	.31	.45
Microstructure R_{Ge}	.19	.21

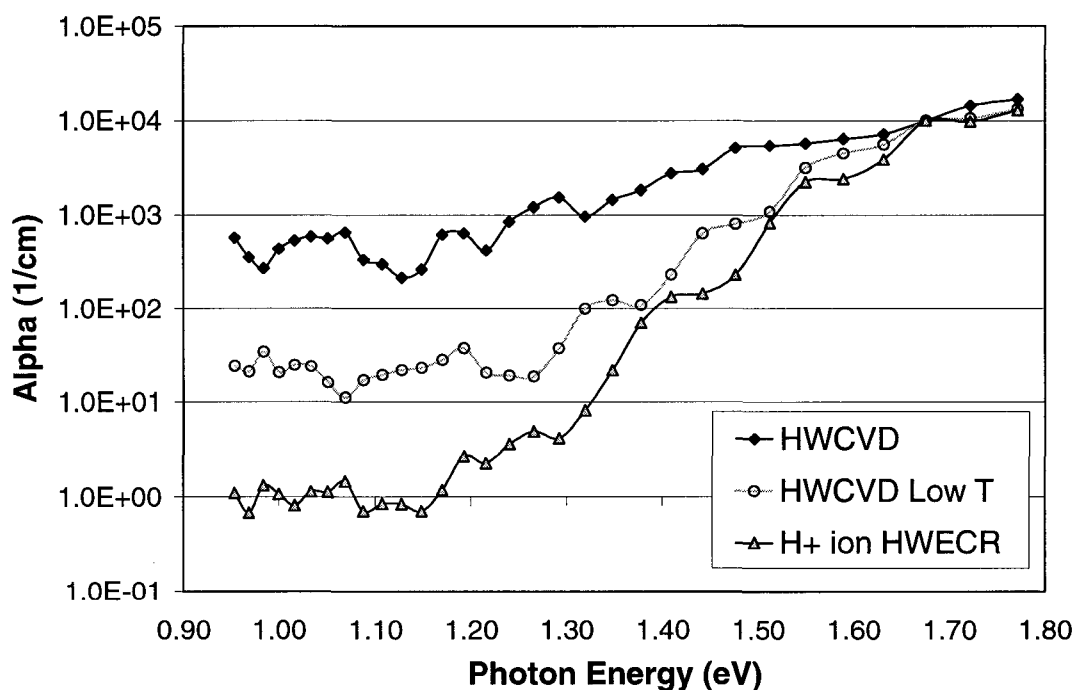## Sub band-gap spectra for 1.55 ev Tauc Gap Materials

Figure 4.4: Sub band-gap absorption spectra for 1.55 eV Tauc's gap material deposited while keeping substrate temperature and chamber pressure constant

ensued. The more ordered structure then resulted in better material properties, as evidenced in table 4.4. Figure 4.4 is a sub band-gap spectrum comparison among the three films shown in the previous two tables. Note the decrease in mid-gap absorption coefficient as first filament temperature is lowered, then ions added. This shows that in addition to the effects of lowered filament temperature and hydrogen dilution, the addition of ions to the reactive mixture further improves the material, as postulated by Robertson's model [18].

4.1.4: E_{Tauc} = 1.45eV material

The lower the band-gap of the material, the more difficult it becomes to deposit the material at growth rates above 1 ang/sec and maintain properties of a high quality material. With this material, the filament temperature was again varied to obtain the best possible material. In addition, the substrate temperature was varied in an attempt to optimize the material parameters. High quality material was deposited by hydrogen plasma HW-ECR material. No material that approached the same characteristics of the ion bombarded material was produced. At this band-gap

Table 4.5: Summary of E_{Tauc} = 1.45eV material grown by H_2 Plasma HWECR

MATERIAL	HW-ECR 250°C
σ_{Photo} (S/cm)	1.4×10^{-6}
$\sigma_{Photo}/\sigma_{Dark}$ Ratio	4.7×10^3
E_{ov} (meV)	47
$\alpha(1.1eV)$ (cm^{-1})	5
Act. Energy (eV)	0.78

the filament temperature was ~300°C lower than used to deposit the a-Si:H material discussed earlier. The decrease in filament temperature resulted in a substantial decrease in deposition rate, and thus the amount of material deposited by PECVD and HWCVD was only 30% different. This could account for the inability to deposit quality material by HWCVD alone. Other groups have reported difficulty depositing material with band gaps this low, and they needed to reduce filament temperature to obtaining materials that were useable [47,48]. In these previous studies, however, the reactor geometry was substantially different. The 1.45eV film that was grown by HW-ECR had photo-conductivity and light to dark ratios that equaled NREL's material, which used a substantially smaller filament to decompose the gases [48]. This had the effect of reducing the zone around the filament where decomposition could occur, and effectively increased the PD product. In the HW-ECR reactor, there is already a large distance between the filament and substrate, however since lower pressures are used in the combined reactor, equivalent PD products were used to produce each material. The HW-ECR material had a lower Urbach energy at 47 meV than the NREL material, which is reported as having an urbach energy of 53 meV [48].

4.2: ECR Plasma Effects

The effects of plasma power, and thus the ion energy and density, was studied for some of the band-gap materials studied. The effects of plasma power on the photo to dark conductivity ratio and the Urbach energy of HW-ECR materials was studied, and some interesting results were observed.

In the 1.65eV Tauc's gap material, a definite trend where Urbach energy decreased with increasing plasma power was observed and is shown as figure 4.5. This trend is expected, because more excess hydrogen would be removed as more

Urbach Energy vs. Plasma Power for 1.65 ETauc Material
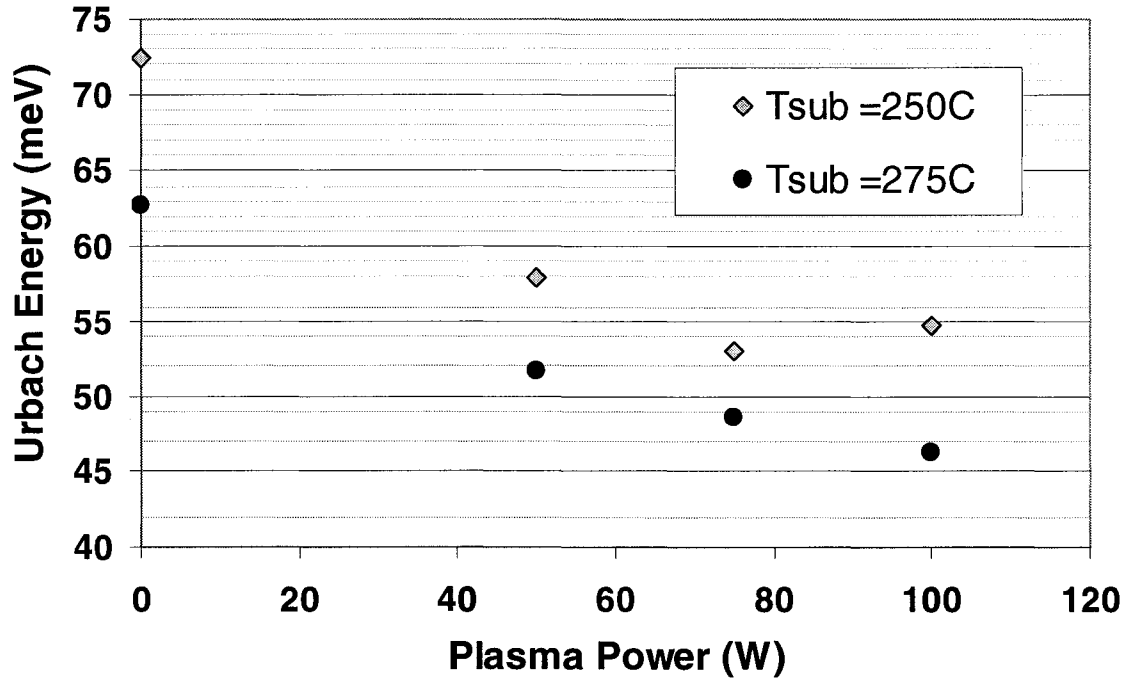
Figure 4.5: Urbach energy decreasing with increasing plasma power in 1.65 eV materials

deposited by HW-ECR using He plasma

ions are present with sufficient energy to break surface hydrogen bonds. This trend was observed with materials deposited using He plasma, not hydrogen plasma, which from other results would undoubtedly yield better results.

Similarly, the photo to dark conductivity ratio improves with increasing plasma power. Figure 4.6 shows these results for three band gaps of a-SiGe:H material. The 1.65 eV material shows a definite increase in photosensitivity with increasing power. The other band-gap materials also exhibited some degree of improvement in both photosensitivity and photoconductivity with the addition of plasma power, as shown in figures 4.6 and 4.7, respectively. The lower band gap materials do not require as much ion energy to create good material, because there is an increase in

Photosensitivity vs. Plasma Power
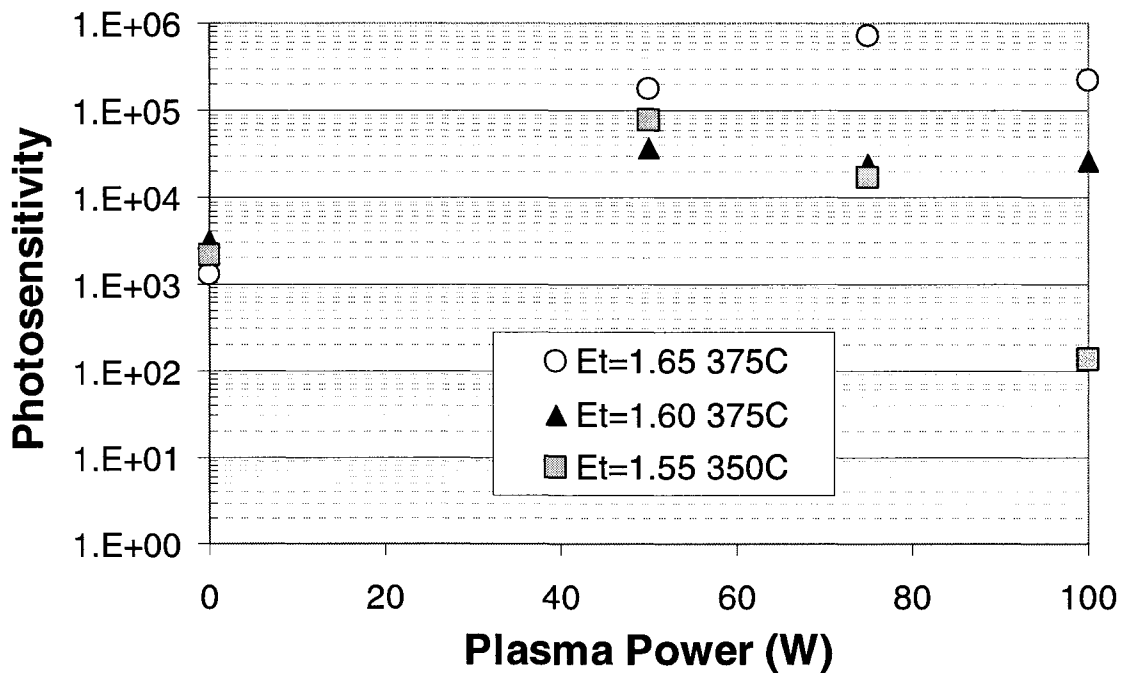
Figure 4.6: Photo to dark conductivity ratio as a function of plasma power for three band-gap materials deposited by HW-ECR [46]

the amount of germanium incorporated into the film, which has lower bond energies with hydrogen; therefore fewer, less energetic ions will help to remove excess hydrogen efficiently. In addition, the filament temperature was held constant through these experiments, and therefore the etching action of hydrogen radicals produced by the hot filament would aid with the effective removal of excess hydrogen.

The photoconductivity values of the materials follow a similar trend as the photosensitivity. The higher gap materials require more plasma energy to produce a high photoconductivity, where less energy is required in the lower gap material. Following a similar argument, the removal of excess hydrogen during deposition is easier for the lower gap material, and therefore less energy in the form of ion bombardment is required to generate high photoconductivity values.

Photoconductity vs Plasma Power for Various Bandgap a-(Si,Ge):H
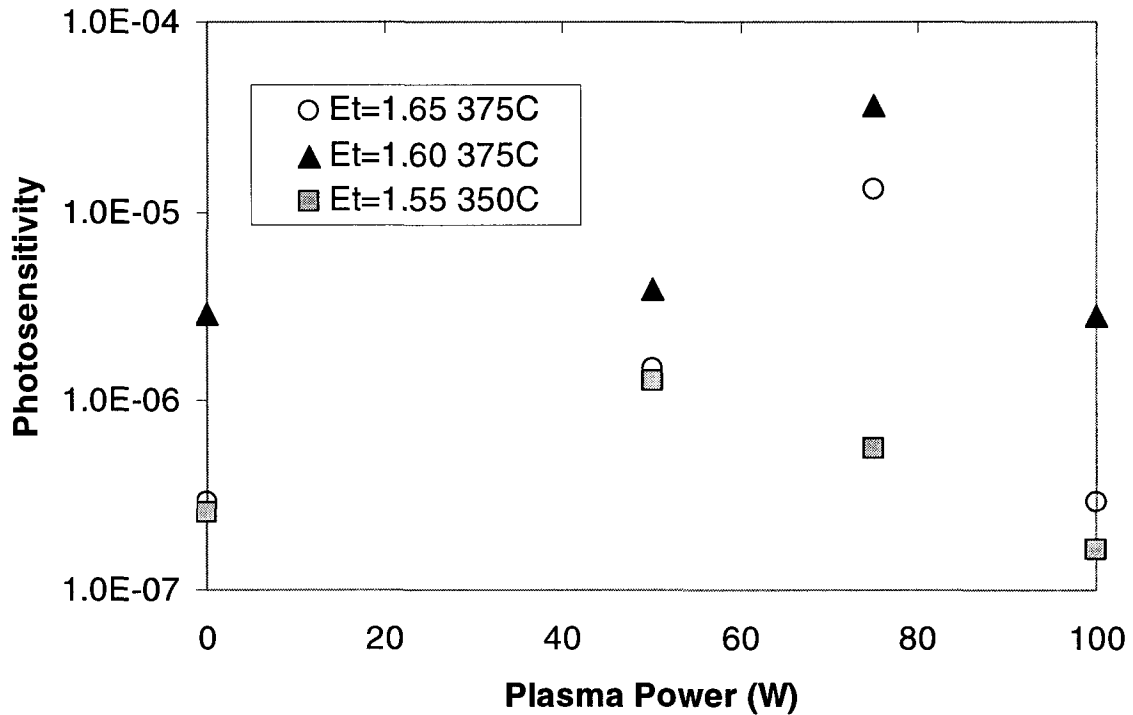
Figure 4.7: Photoconductivity as a function of plasma power for three band-gap material deposited by HW-ECR using He plasma

The result obtained by increasing the ion bombardment energy and density is consistent with literature. There have been reports of degradation in a material's physical and electrical properties after increasing the ion bombardment energy beyond an optimal value [12]. The HW-ECR materials exhibit that same quality, which can be readily seen in figures 4.6 and 4.7 as the lower gap materials reach their optimum at lower values of plasma power and then degrade as more plasma power is added. It seems that the effect of the ions impacting the growing film surface is changing from removing excess hydrogen to removing the hydrogen and

imparting damage to the growing structure. For example, it is easy to imagine a He ion that has enough energy to not only break a weak Si-H bond, but to also continue into the matrix and disrupt a Si-Si bond or even remove slightly interior hydrogen and introduce a dangling bond. The optimization of the density and energy of the impacting ions is the key to high quality material.

In materials with 1.55eV Tauc gap and lower, hydrogen plasma was used instead of He plasma. The hydrogen is a reactive species in this deposition reaction, so the exact nature of its role is more ambiguous than the He ions, which can only impart energy through collision. The hydrogen plasma materials exhibited excellent properties, but yet the growth rates were similar to the growth rates of the He plasma materials. There are three possible explanations for this behavior. First, since hydrogen is a smaller atom, it can penetrate further into the lattice to remove more excess hydrogen like Robertson's model postulates [18]. Second, the hydrogen may be passivating buried dangling bonds as it makes its way into the growing film, thus reducing defect density and improving the overall quality of the material. Third, due to the reactive nature of the hydrogen, it is likely much more effective at breaking surface Si-H bonds than He is, as the energy of the ion only needs to overcome the energy required to form the transition state from a Si-H bond to a H-H bond, and not the entire Si-H bond energy. Therefore, a lower power H_2 plasma produces a larger density of H^+ ions that have enough energy to remove surface hydrogen, but not to impart impact damage to the growing matrix. These properties make the hydrogen plasma ideal for depositing low-gap materials that are very sensitive to ion damage due to the low energy of the Ge-H bond.

4.3: Filament Temperature Effects

In order to deposit high quality hydrogenated low-gap silicon germanium alloys, it was necessary to reduce the filament temperature from the ~2200°C used for a-Si:H deposition to ~1900°C. With the reduction in filament temperature, an improvement in the quality of ETauc = 1.55 eV material deposited by HW-ECR CVD was seen, however, the analogous material deposited by HWCVD was unchanged.

Table 4.6: Comparison of E_{Tauc} = 1.55eV materials grown by HWCVD at different filament temperatures with hydrogen dilution

MATERIAL	T_{fil} = 2200°C	T_{fil} = 2100°C
σ_{Photo} (S/cm)	6.4×10^{-7}	5.2×10^{-7}
σ_{Dark} (S/cm)	6.4×10^{-11}	5.4×10^{-11}
$\sigma_{Photo}/\sigma_{Dark}$ Ratio	1.0×10^{4}	9.7×10^{3}
E_{Act} (eV)	0.83	0.84
E_{ov} (meV)	51	51
α(1.1eV) (cm^{-1})	17	20
Microstructure R_{Si}	.45	.45
Microstructure R_{Ge}	.25	.21

Table 4.6 shows a comparison between two films deposited by HWCVD under the same dilution, substrate temperature, and gas flow conditions; but varying in the temperature of the catalyzing filament. There is little observed difference between the two materials, however, which is puzzling. According to the MGP model, a decrease in deposition rate should improve the material; however the 30% reduction in growth rate did not affect the material. The increase in time between silyl addition

events provided by this lower deposition rate should allow for more excess hydrogen to be removed, thus improving the material quality.

When hydrogen plasma ions are added to the deposition chemistry, we see a different picture emerge when the filament temperature is decreased. As table 4.7 shows, reducing the filament temperature increases the photo-conductivity, the

Table 4.6: Comparison of $E_{Tauc} = 1.55eV$ materials grown by HW-ECR CVD at different filament temperatures with hydrogen plasma

MATERIAL	$T_{fil} = 2200°C$	$T_{fil} = 2100°C$
σ_{Photo} (S/cm)	2.8×10^{-6}	5.4×10^{-6}
σ_{Dark} (S/cm)	7.3×10^{-11}	8.2×10^{-11}
$\sigma_{Photo}/\sigma_{Dark}$ Ratio	3.8×10^{4}	6.6×10^{4}
E_{Act} (eV)	0.82	0.82
E_{ov} (meV)	47	44
$\alpha(1.1eV)$ (cm^{-1})	10	0.9
Microstructure R_{si}	.26	.17

photo to dark conductivity ratio, and decreases both the Urbach energy and sub band-gap absorption coefficient of the material. These results indicate that a reduction in filament temperature affects the deposition chemistry in a way that is beneficial to the resulting material. But what is occurring when the filament temperature decreases?

At even lower band-gaps further reduction in filament temperature was required to deposit materials using either method. However, as the filament temperature is reduced for these low gap materials, and decrease in the band-gap of

the HWCVD materials is observed, as shown in figure 4.8. The band-gap of the HW-ECR material stays relatively constant while a decrease in band-gap is seen in the HWCVD materials. The reactivity of the filament has been reported to become much less effective for silane at lower temperatures [24], and this lower reactivity may be the cause for the decrease in the band-gap as less silicon is decomposed and incorporated into the material as filament temperature decreases. The HW-ECR material would maintain a higher band-gap because hydrogen ions would decompose the silane as they would in PECVD; supplying the required silyl radicals for adding silicon to the deposited material. As the decomposition probability of

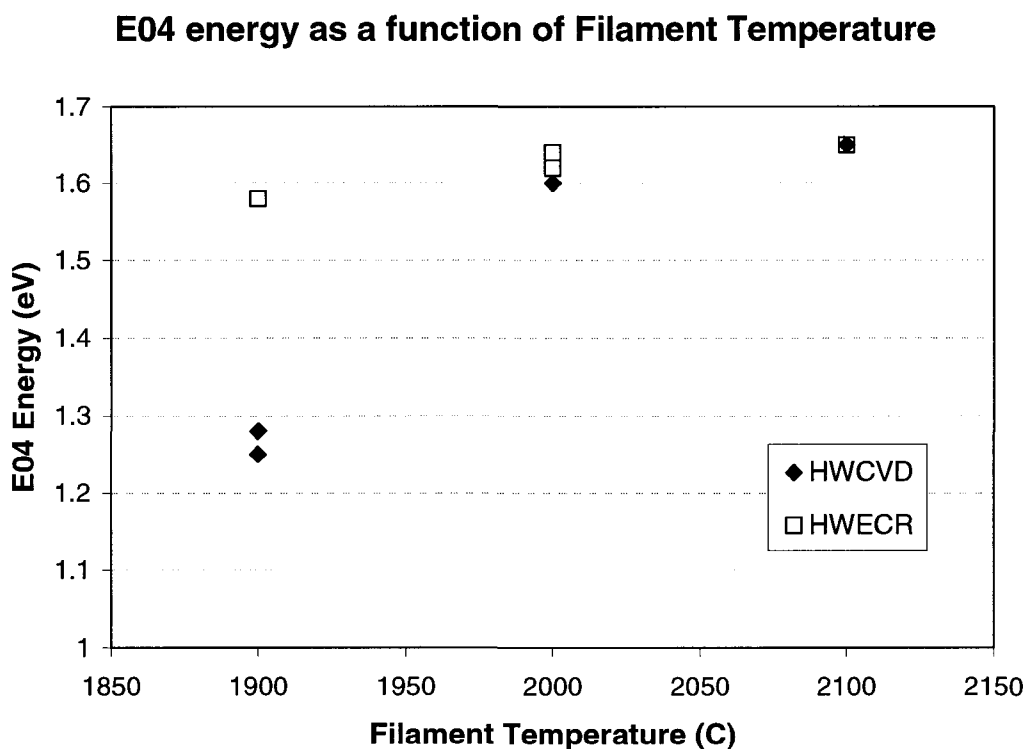**E04 energy as a function of Filament Temperature**

Figure 4.8: Reduction in band-gap of materials grown under identical conditions except for a reduction in filament temperature

silicon decreases, the decomposition probability for germane is little-changed , and fewer hydrogen radicals are available for hydrogen abstraction.

The reduced dissociation probability of silane as filament temperature decreases is beneficial to the MGP model, as it would promote the production of silyl radicasl either directly through incomplete decomposition or by reducing the amount of silane decomposed by the filament allowing the production of silyl radicals through the addition of hydrogen radicals to silane molecules as shown by equation 2.2 on page 15 of this dissertation. Whatever the physical reason for the reduced incorporation of silicon into the material, the reduced filament temperature is required for depositing high quality HW-ECR materials at lower band-gaps.

4.4: Photovoltaic Device Results

Photovoltaic devices containing i-layers deposited by the HW-ECR process were fabricated for comparison against conventional PECVD devices. The actual device deposition process consisted of depositing a PECVD n^+ layer, then the HWECR intrinsic layer, followed by an intrinsic buffer layer and a p+ layer both deposited by ECR-PECVD. This process required two air breaks, which is not an optimum process, however the HW-ECR reactor cannot deposit doped materials, as the required gases are not presently connected to the system. The following results show that the HWECR solar cells are close in performance to the PECVD cells deposited by this research group. While there is still a problem with the device series resistance, the quantum efficiency data shows comparable performance to the best a-Si:H devices deposited entirely by ECR-PECVD.

4.4.1: J-V Results

The current voltage characterization of the a-Si:H devices deposited by HW-ECR show a problem with the internal series resistance of the device. The series resistance problem is most likely a process problem concerning the interface with the top p-layer of the device, as it is critical to have a smooth graded transition here to prevent the blocking of holes from entering into the p-layer for collection. Work is ongoing to optimize the process and show a J-V curve that is on par with the best thin film devices. Figure 4.9 shows the current J-V characteristic of an a-Si:H device deposited with a HW-ECR intrinsic layer. The device shows a rounded transition when compared to a recent PECVD device as shown in figure 4.10, indicating the increased series resistance of the HWECR device.
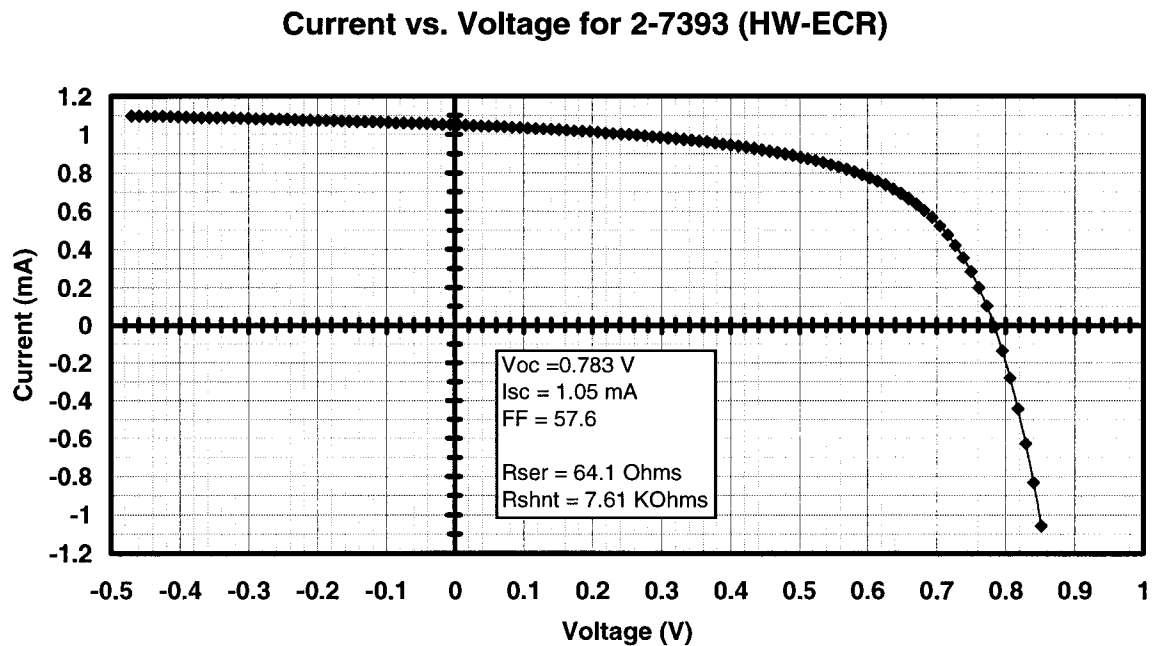
Current vs. Voltage for 2-7393 (HW-ECR)

Figure 4.9: Sample J-V curve for an a-Si:H device with a HW-ECR i-layer

Current vs. Voltage for 2-7379

Voc =0.761 V
Isc = 0.684 mA
FF = 62.73

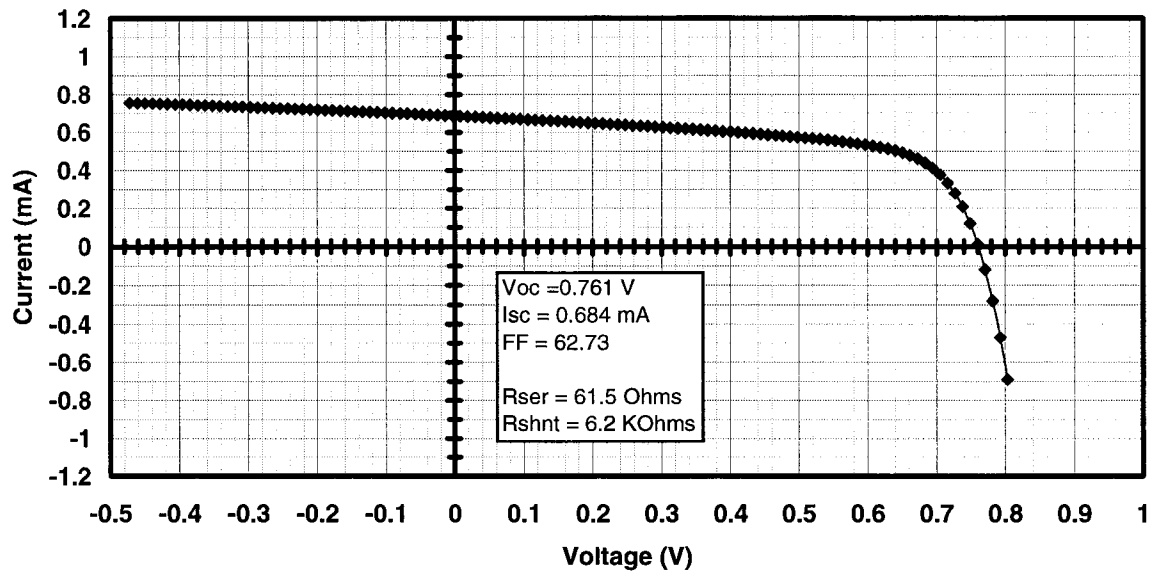Rser = 61.5 Ohms
Rshnt = 6.2 KOhms

Figure 4.10: Sample J-V curve for an a-Si:H ECR-PECVD solar cell

The cell described by figure 4.9 does have a higher open circuit voltage and a higher short circuit current than the PECVD device shown in figure 4.10. The increase in short circuit current probably arises from the 30% increase in thickness that the HW-ECR device has over the PECVD device. The fill factor on the ECR-PECVD device is substantially better than the HW-ECR device, however when the series resistance is optimized, the fill factors should be comparable.

4.4.2: Quantum Efficiency Results

While the I-V characteristics of the two devices are different due to the series resistance problem of the HW-ECR device, the quantum efficiency result are quite similar for the two devices, indicating that the basic device structures are sound and materials are of the same quality. Figure 4.11 shows the quantum efficiency spectra
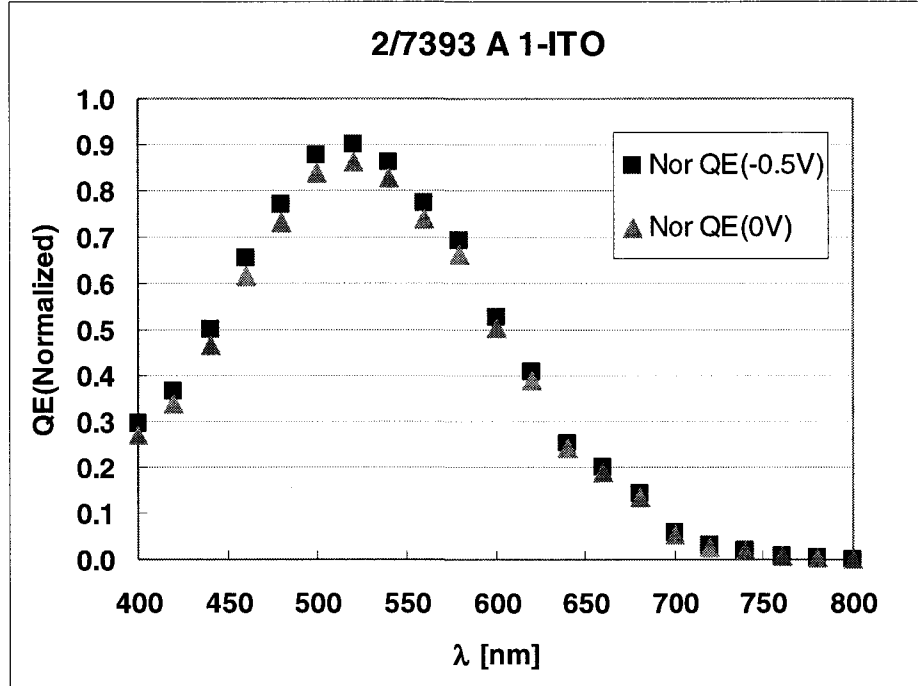
72

2/7393 A 1-ITO

Figure 4.11: QE results of a-Si:H device with HW-ECR i-layer

2/7379-A3 ITO
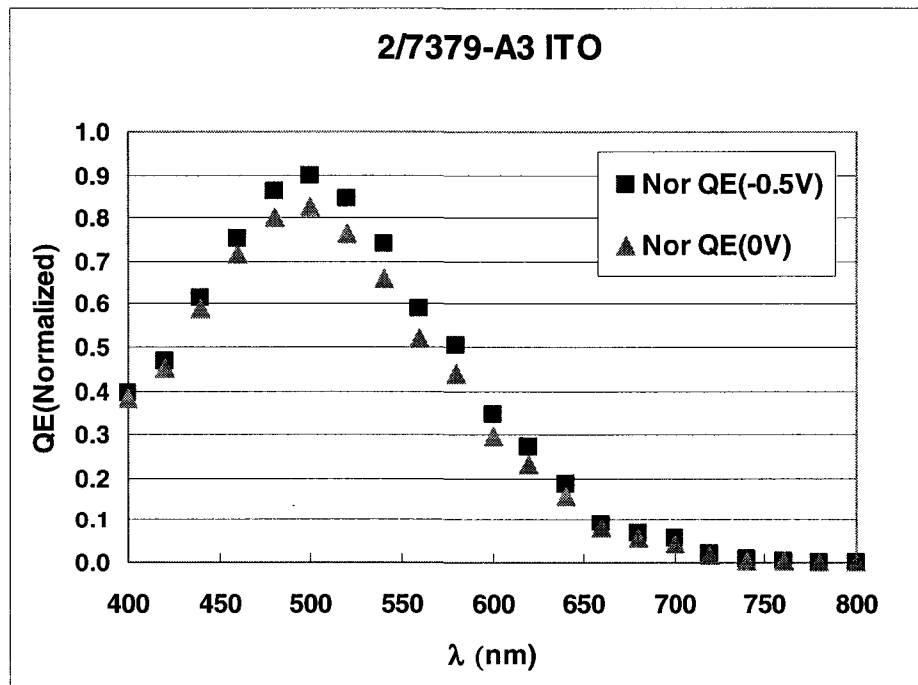
Figure 4.12: QE results of ECR-PECVD a-Si:H device

of the HW-ECR device while figure 4.12 shows the QE results of the ECR-PECVD device. Due to the increased thickness of the HW-ECR device, a slight shift to longer wavelengths is seen when compared to the PECVD device. The device thickness also causes the QE peak to be slightly wider throughout its breadth. The PECVD device has enhanced low wavelength QE as seen by the value of the relative QE at 400 nm. In general enhanced QE at longer wavelengths is required for solar cells as that is where largest intensity of energy in the solar spectrum that falls on earth is located.

The difference in QE is slight and indicates that the HW-ECR device is better for photovoltaic applications, although no light degradation studies have been performed. The wider QE peak indicates enhanced carrier collection over a wider

QE Ratio Spectra

Figure 4.13: QE ratio as a function of wavelength for ECR and HW-ECR devices

range of wavelengths. This difference may be due to the thicker absorption layers in the HW-ECR device when compared to the PECVD device, however.
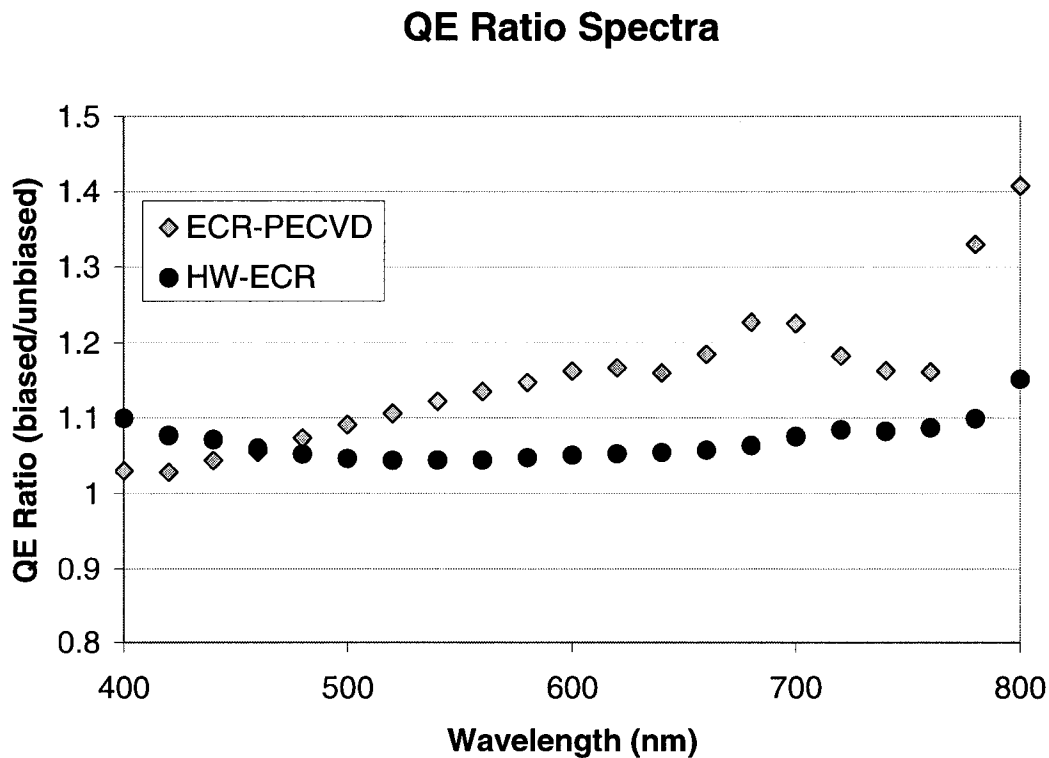
The QE ratio spectrum of biased QE vs. unbiased QE is ~1.1 for the HW-ECR solar cell as is shown in figure 4.13. The HW-ECR cell performs better than the ECR-only cell that is used for comparison here, however typical ECR-PECVD devices have ratios which stay below 1.2 at all wavelengths. The QE ratio confirms that the material deposited for the i-layer of the HW-ECR device has a low defect density. Since the material grown on 7059 glass had a low E_{OV}, we assume that it has a low defect density in its band-tails and in the mid-gap region. And, since the material is assumed to have few defects, then there should be a high electric field in the i-layer of the device which will cause carrier transport to be field-limited rather than diffusion-limited, making the QE ratio of the device close to one. Since the measured QE ratio of the device is near 1.1 throughout the wavelength range, the data is self-consistent and the material must have a low defect density.

CHAPTER 5: CONCLUSIONS

The objective of this research is to show the effects of ion bombardment on the quality of a-(Si,Ge):H materials by using a novel combined hot-wire and remote electron cyclotron resonance (ECR) plasma reactor. The data obtained from comparing material deposited with and without ions present are used to suggest improvements to the standard deposition model outlined by Matsuda [1], Gallagher[2], and Perrin [3] (the MGP model) to account for the effects of ion bombardment. Also, the first ever photovoltaic devices containing i-layers deposited by this novel technique were to be deposited. In the following chapter, conclusions regarding the improvement of physical properties ion bombardment makes; what modifications should be added to the MGP model to reconcile it with the fact that high ion bombardment condition deposit quality materials; and the performance of HW-ECR photovoltaic devices are presented. In addition, suggestions for future research will be presented.

5.1: HWCVD and HW-ECR Materials

From the results presented in chapter 4, it appears that the addition of ion bombardment to the HWCVD process produces materials with high quality at lower temperatures than with HWCVD alone. The a-(Si,Ge):H materials deposited by HW-ECR exhibit properties more suited for photovoltaic applications than the HWCVD material grown at the same substrate temperatures. In addition, many of the materials deposited with the HW-ECR method showed properties that were radically better than their HWCVD counterparts. The addition of ion bombardment, whether He or H_2 plasma ions, improves the material. This result indicates that not only penetrating hydrogen ions which aid in the removal of excess hydrogen during

growth improve the material; but that neutral ions, capable of imparting energy to the material through impact energy alone, aid in the production of high quality materials.

At all band-gaps studied, ion bombardment produced better material. At the lowest band-gaps studied, materials produced by HW-ECR were much better than films deposited without ions. The drawback to HW-ECR is the reduction in growth rate. A higher throughput reactor needs to be fabricated in order to study the effects of ion bombardment at even higher growth rates. All the materials were deposited at growth rates of ~1 Å/sec. or greater, placing them in the realm of high growth rate materials.

5.2: Adaptations to the MGP Model

Since ion bombardment definitely improves the material quality of a-Si:H and a-(Si,Ge):H, the MGP model is not complete and needs to include the effects of ion bombardment. As discussed in Chapter 1, John Robertson of Cambridge University has developed a model for the role of hydrogen ions in the deposition process that involves the spinodal decomposition of the material and the hydrogen ions penetrating the material matrix and removing the hydrogen in the form of an H_2^* group that diffuses readily to the material surface and out, thus removing it from the material [18]. The material quality-limiting process is the removal of excess hydrogen, and through Robertson's model, a pathway for that process involving hydrogen ions is put forward.

In this research, bombardment of the growing film by hydrogen ions improved the material drastically. In addition, when compared to a film where helium ions were used, the films grown using hydrogen ions exhibited much better properties, indicating that non-reactive ions aid in film growth in a different manner than the reactive hydrogen species. The hydrogen is much more efficient at removing

excess hydrogen from the growing material than the He ions. Robertson's model [18] is supported by these results as the model depends upon the bonding of the hydrogen ion to interior hydrogen and the out-diffusion of the resulting complex. Helium ions could not bond to an interior hydrogen and promote this hydrogen removal, so hydrogen ions should effect a greater improvement in the material properties than helium.

In addition to the interior removal of hydrogen, the H^+ ions can also remove surface hydrogen much like atomic hydrogen can within a certain "growth zone" in the outer few atomic layers of the material. Robertson proposes this behavior also, and it is intuitive due to the energetic and reactive nature of the H^+ ions. This is similar to the proposal of Dalal [4], where he theorizes that ions can break "wing-bonded" hydrogen that is bound at the sides of added silyl radical, rather than projecting out from the surface. The hydrogen bound at the surface are readily removed by other abstraction methods, such as the MGP model's postulated silyl radical abstraction. This view of the surface reaction chemistry is consistent not only with results generated here, but also with empirical results of PECVD depositions of microcrystalline silicon and alloys. In these materials, a large density of hydrogen ions is required to form nucleation sites and deposit high quality materials. The high hydrogen dilution causes a large flux of ions to be incident on the deposited film surface, where weakly bound hydrogen can be removed permitting nucleation of a crystalline phase. After this nucleation, the hydrogen dilution can be eased as there is no longer any interior hydrogen in the crystallites, only in the amorphous tissue surrounding the crystallites. Thus, after nucleation and initial growth, only enough hydrogen ions are needed to remove interior excess hydrogen from the interstitial a-Si:H regions. Like any feasible growth model, this model is consistent with similarly deposited a-Si:H and nanocrystilline silicon.

He ion
bond-breaking

He ion diffusion
enhancement

H ion bond
breaking

H ion interior
Excess hydrogen
removal
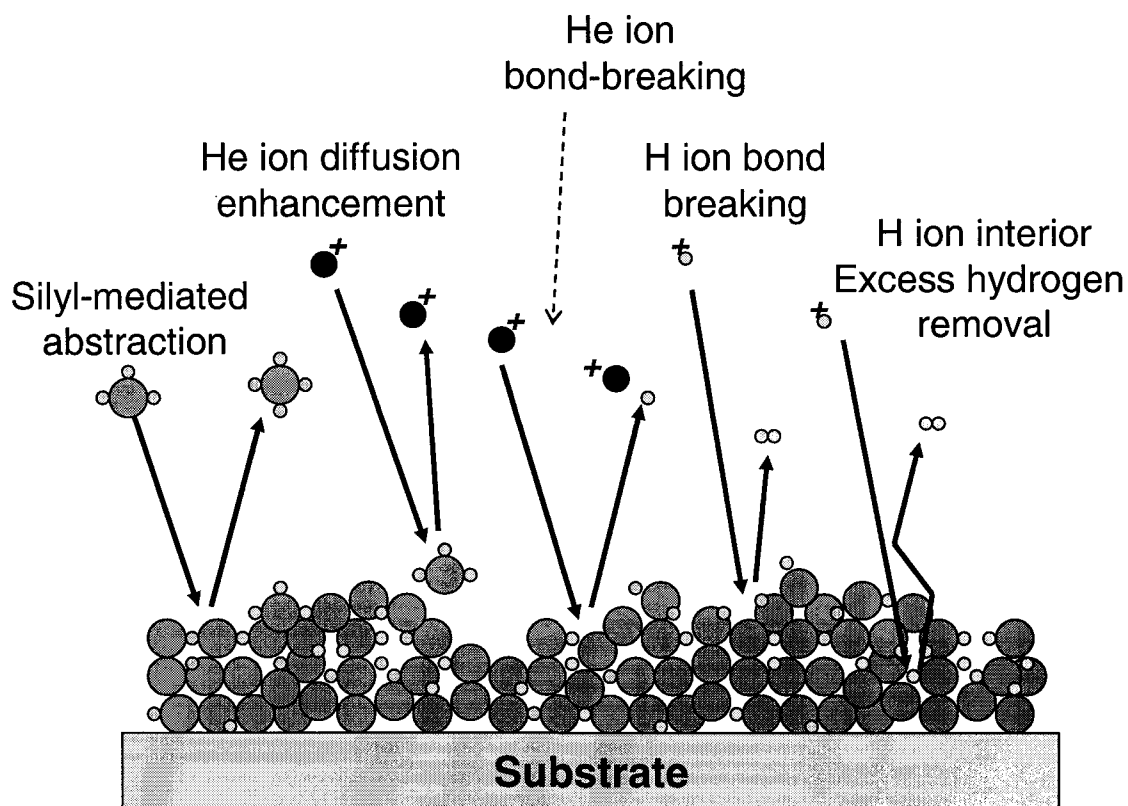
Silyl-mediated
abstraction

Substrate

Figure 5.1: Schematic diagram representing postulated methods of excess hydrogen removal in the growth of hydrogenated silicon-germanium alloys in environments with ions present

An improvement is seen when He ions are used compared to the HWCVD materials, so the helium ions must play a role in deposition chemistry. The most probable role for the helium ions is the enhancement of surface mobility of the ad-radicals during deposition. The enhancement of the surface mobility of the germyl and silyl radicals will promote a more uniform surface growth and a reduction of included defects. The helium ions may also contribute to the removal of surface hydrogen through physical etching of the weak bonds at the surface, and like the hydrogen ions, in a "growth zone" just below the surface. The growth zone for the

helium ions would be narrower than for hydrogen ions, however, as the larger ions would contact a radical or bound hydrogen before penetrating into the film very far.

So how can these ideas be reconciled with the standard MGP growth model? The effects of ions can be simply added in addition to the existing model. It is wholly reasonable that SiH_3 is the main radical responsible for deposition of quality hydrogenated amorphous silicon-germanium alloys, and the process of silyl-mediated hydrogen abstraction is possible, so the effect of ions is to offer other pathways for the removal of excess hydrogen. Figure 5.1 summarizes the methods of excess hydrogen removal in this growth model, while still maintaining that film growth arises from the addition of mainly silyl radicals.

5.3: HW-ECR Photovoltaic Devices

The first ever solar cells with i-layers deposited by HW-ECR have been fabricated at Iowa State University. These devices show that this novel process can produce photovoltaic material that is as good as other methods and produces the devices at high growth rates. While the devices are still limited by the air-breaks inherent in the process design, with careful optimization, the series resistance of the HW-ECR devices will be reduced and the I-V curve will be comparable to the best ECR-PECVD devices. Presently, the quantum efficiency of the HWECR devices shows reduced low wavelength values, but increased breadth of the QE peak, and a slight shift to lower wavelengths. This enhanced carrier collection at lower wavelengths makes the HW-ECR devices well suited to photovoltaic applications. When the series resistance problem is resolved, the devices will be of exceptional quality and efficiency.

5.4: Future Research Directions

Further efforts should be spent looking at the effect of reduced filament temperature on the deposition chemistry. The difference in decomposition probability between germane and silane is interesting and a more precise study of this reaction should be undertaken.

Pushing the growth rate of low-gap materials to higher levels should be investigated by using a less-dilute germane-hydrogen mixture for supplying the germane to the reactor. The 9:1 dilution of germane gas prevented the total flow rate of reactive gases (SiH4 and GeH4) from being over 5 sccm in the process used for depositing the lowest gap materials. In contrast, a-Si:H was deposited using 12 sccm of silane, and thus had a seven times greater deposition rate. By studying the higher growth rate HW-ECR material, it can unambiguously show the effects of ion bombardment.

A computer simulation that takes into account the effects of ion bombardment should be developed to probe further the exact effect of ions in the deposition chemistry. Many papers have studied molecular dynamic simulations of the MGP model, one that examines Robertson's model would be a nice comparison.

Finally, some effort should be put into applying the HW-ECR process to large-area depositions. The ability to reduce substrate temperature would make it even easier to deposit on temperature-sensitive materials, even though some groups are already using HWCVD to deposit a-Si:H on plastics and other substrates in large area applications.

REFERENCES

[1]   A. Matsuda, et. al., "Guiding principle in the preparation of high-photosensitivity hydrogenated amorphous SiGe alloys from glow-discharge plasma," Japan. J. Appl. Phys. **25**, 54 (1986)

[2]   A. Gallagher, "Neutral radical deposition from silence discharges," J. Appl. Phys.,**63**, 2406 (1988)

[3]   J. Perrin, et. al., "Surface reaction probabilities and kinetics of H, SiH_3, Si_2H_5, CH_3, and C_2H_5 during deposition of a-Si:H and a-C:H from H_2, SiH_4, and CH_4 discharge," J. Vac. Sci. and Tech., **A16**, 278 (1998)

[4]   V. Dalal, "Fundamental considerations regarding the growth of amorphous and microcrystalline silicon and alloy films," Thin Solid Films **395**, 173 (2001).

[5]   V. Dalal, S. Haroon, Z. Zhou, T. Maxson, and K. Han, "influence of plasma chemistry on the properties of a-(Si,Ge):H alloys," J. Non-Cryst. Solids, **266-269**, 675 (2000)

[6]   J.Zhu, et. al., "Growth and properties of amorphous Ge:H solar cells," J. Non-Cryst. Solids, ICAMS 20 proc., *To Be Published*

[7]   Nelson, B. et al, " Hydrogenated amorphous silicon grown by hot-wire CVD at deposition rates up to 1 µm/minute," Mat. Res. Soc. Symp. Proc., **609**, A22.8.1 (2000)

[8]   Jadakar, S. et al, " The effect of substrate temperature on HW-CVD deposited

a-SiGe:H films," J. Non-Cryst. Solids, **299-302**, 168 (2002)

[9]   V. Dalal, P. Seberger, M. Ring, and P. Sharma, "Growth and properties of a-Si:H films grown with combined cat-CVD and ECR-plasma techniques," Thin Solid Films, **430**, 91 (2003)

[10]   R. Dewarrat and J. Robertson, "Binding and surface diffusion of SiH_3 radicals and the roughness of hydrogenated amorphous silicon," App. Phys. Lett. **82**, 883 (2003)

[11]   W.M.M. Kessels, M.C.M. van de Sanden, R.J. Severens, and D.C. Schram, "Surface reaction probability during fast deposition of hydrogenated amorphous silicon with a remote silane plasma," J. Appl. Phys., **87**, 3313 (2000)

[12]   H. Aguas, R. Martins, and E. Fortunato, "Role of ion bombardment on the properties of a-Si:H films," Vacuum, **60**, 247 (2001)

[13]   T. Sasaki and Y. Ichikawa, "Effect of ion bombardment during plasma CVD on the film properties of a-Si:H studied by IEC plasma CVD," J. Non-Cryst. Solids, **198-200**, 1007 (1996)

[14]   S. Will, H. Mell, M. Poschenrieder, and W. Fuhs, "a-Si:H deposited at high rate on the cathode of a rf-PECVD reactor," J. Non-Cryst. Solids, **227-230**, 297 (1998)

[15]   G. Parsons, C. Yang, T. Klein, and L. Smith, "Reaction processes for low

temperature (<150C) plasma enhanced deposition of hydrogenated

amorphous silicon thin film transistors on transarent plastic substrates," Mat.

Res. Soc. Symp. Proc., **507**, 19 (1998)

[16]   P. Roca i Cabarrocas, "Detailed study of ion bombardment in rf glow

discharge systems: role of helium dilution," Mat. Res. Soc. Symp. Proc.,

149, 33 (1989)

[17]   W.C. Weller and G.H. Bauer, " Correlation between microstructure and

optoelectronic properties of a-Ge:H," Mat. Res. Soc. Symp. Proc., **149**,

339 (1989)

[18]   J. Robertson, "Growth mechanism of hydrogenated amorphous silicon," J.

Non-Cryst. Solids, **266-269**, 79, (2000)

[19]   E.C. Molenbroek, A.H. Mahan, A. Gallagher, "Mechanisms influencing "hot-

wire" deposition of hydrogenated amorphos silicon," J. Appl. Phys. **82**, 1909

(1997).

[20]   H. Matsumura, "High quality amorphous silicon prepared by catalytic chemical

vapor deposition (CTL-CVD) method," Mat. Res. Soc. Symp. Proc. **95**, 261

(1987).

[21]   Q. Wang, E. Iwaniczko, J. Yang, K. Lord, S. Guha, "High quality amorphous silicon germanium alloy solar cells made by hot-wire CVD at 10 Å/s," Mat. Res. Soc. Symp. Proc. **664**, A7.5.1 (2001).

[22]   A.H. Mahan, M. Vanecek, A. Poruba, V. Vorlicek, R.S. Crandall, and D.L. Williamson, "Low defect density microcrystalline-Si deposited by the hot wire technique," Mat. Res. Soc. Symp. Proc. **507**, 825 (1998).

[23]   Q. Wang, E. Iwaniczko, A.H. Mahan, D.L. Williamson, "Microcrystalline silicon n-i-p solar cells deposited entirely by the hot-wire chemical vapor deposition technique," Mat. Res. Soc. Symp. Proc. **507**, 903 (1998).

[24]   A. Gallagher, "Some physics and chemistry of hot-wire deposition," Thin Solid Films **395**, 25 (2001).

[25]   M. Ichikawa, J. Takeshita, A. Yamada, and M. Konagai, "Hydrogen dilution effect of the crystallinity of silicon films grown by hot wire cell method," Mat. Res. Soc. Symp. Proc. **557**, 531 (1999).

[26]   V. Dalal, "Growth Chemistry of Amorphous Silicon And Amorphous Silicon-Germanium Alloy," Current Opinion in Solid State *In Press*.

[27]   R. Geller, Electron Cyclotron Resonance Ion Sources and ECR Plasmas, Institute of Physics Publishing, Philadelphia, 1996.

[28] S. DeBoer, "Low temperature epitaxial silicon growth using electron-cyclotron resonance plasma deposition," Ph.D. Dissertation, Iowa State University, 1995.

[29] M. Pontoh, "ECR plasma analysis: correlation between plasma conditions and growth rate," M.S. Thesis, Iowa State University, 2002.

[30] S. Sivaram, Chemical Vapor Deposition: thermal and Plasma Deposition of Electronic Materials, Van Nostrand Reinhold, New York, 1995.

[31] R.A. Powell, ed., Dry Etching for Microelectronics, Elsevier Sci. Pub. Co., New York, 1984.

[32] Y. Liu, "High growth rate deposition of hydrogenated amorphous silicon-germanium films and devices using ECR-PECVD," Ph.D. Dissertation, Iowa State University, 2002.

[33] A. Sherman, Chemical Vapor Deposition for Microelectronics: principles, Technology, and Applications, Noyes Publications, 1987.

[34] P. Seberger, "Novel Techniques for growth of amorphous silicon," M.S. Thesis, Iowa State University, 2002.

[35] M. Ring, "Growth and characterization of hydrogenated amorphous silicon prepared using a combined hot wire and electron cyclotron resonance plasma deposition technique," M.S. Thesis, Iowa State University, 2003.

[36]   K. Ishibashi, "Development of the Cat-CVD apparatus and it feasibility for
        mass production," Thin Solid Films **395**, 12 (2001).

[37]   F.O. Adurodija, H. izumi, T. Ishihara, H. Yoshioka, and M. Motoyama, "The
        electro-optical properties of amorphous indium tin oxide films prepared at
        room temperature by pulsed laser deposition," Solar Energy Materials and
        Solar Cells, **71**, 1 (2002).

[38]   D.K. Schroder, Semiconductor Material and Device Characterization, John
        Wiley & Sons, Inc. New York, 1998.

[39]   E.C. Molenbroek, A.H. Mahan, E.J. Johnson, A.C. Gallagher, "Factors
        influencing the quality of a-Si:H films deposited by the `hot wire` technique,"
        Mat. Res. Soc. Symp. Proc. **336**, 43(1994).

[40]   D. Staeblar and C. Wronski, "Reversible conductivity changes in discharge
        produced amorphous Si," Applied Phys. Lett. **31**, 292 (1977).

[41]   C.J. Fang, K.J. Gruntz, L.Ley, M. Cardona, F.J. Demond, G.Müller, and S.
        Kalbitzer, "The hydrogen content of a-Ge:H and a-Si:H sample determined by
        IR spectra, gas evolution, and nuclear reaction techniques," J. Non-Cryst.
        Solids. **35&36**, 255 (1980).

[42]   S. Lee, S. Kumar, and C. Wronski, " A critical investigation of a-Si:H photoconductivity generated by sub-gap absorption of light," J. Non-Cryst. Solids **114**, 316 (1989).

[43]   M. Stuzmann, W.B. Jackson, C.C. Tsai, Phys. Rev. B **34**, 63 (1986).

[44]   W. den Boer, "Determination of midgap density of states in a-Si:H using space-charge-limited current measurements," J. de Physique, **42**, C-4, 451 (1981).

[45]   Y. Liu, "High growth rate deposition of amorphous silicon-germanium films and devices using ECR-PECVD," Ph.D. dissertation, Iowa State University, 2002.

[46]   M. Ring, V. Dalal, and K. Murthukrishnan, "Properties of a-Si:H and a-(Si,Ge):H films grown using combined hot wire-ECR plasma process," J. Non-Cryst. Solids, Proc. Of 20th ICAMS, *to be published in 2004*

[47]   B.P. Nelson, Y. Xu, D.L. Williamson, B von Roedern, A. Mason, S. Heck, A.H. Mahan, S.E. Schmitt, A.C. Gallagher, H. Webb, and R. Reedy, "Hydrogenated amorphous silicon germanium alloys grown by the hot-wire chemical vapor deposition technique," Mat. Res. Soc. Symp. Proc., **507**, 447 (1998)

[48] B.P. Nelson, Y. Xu, D.L. Williamson, D. Han, R. Braunstein, M. Boshta, and B. Alavi, " Narrow gap a-SiGe:H grown by hot-wire chemical vapor deposition," Thin Solid Films, 430, 104 (2003)

89

ACKNOWLEDGEMENTS

While working on any project, a person's success can only come with the help of others. I am no different and need to recognize many different individuals for their help with this Dissertation.

First, I need to thank Professor Vikram Dalal, my major professor, for his support and patience during this project. Also, I wish to thank my graduate committee members, Dr. Gary Tuttle and Dr. Alan Constant, Dr. Mani Mina, and Prof. Surya Mallapragada for their guidance during this process. I also need to thank Mr. Max Noack for his help keeping equipment functional as I did my experiments and Ms. Jane Woline for knowing who to talk to for various problems at the MRC.

I also need the thank all of the students out at the MRC who have helped me during the years: Puneet Sharma and Kamal Murthukhrishnan for some DBPC measurements, Kay Han, Nanlin Wang, and Durga Panda for p-i-n characterization, Josh Graves, Micah Decker, Paul Seberger, Jarrod McDonald, Curt Melchert, Jason Xu, Andy Niu, Yong Liu, Marsela Pontoh, Debju, and even Tyson Benson. Thank all of you for your help, support, and friendship.

I need to thank my wife Alica for her moral support of me during this work even while she was working toward her DVM, we made it! Also, I thank my parents and hers for their support during these graduate school years.

Finally, and certainty not least of all, I need to thank the Catron Foundation, the Graduate college, the Dept. of Electrical and Computer Engineering, and the Thomas Whitney Endowment for financial support. Also, I must thank NREL for the financial backing of this research that paid for the materials used throughout. Without this support, I would undoubtedly not be here today, thank you.

APPENDIX 1: HW-ECR REACTOR

Photograph of the HW-ECR reactor showing the control equipment, the vacuum system, the hot-wire power supply, and the gas flow equipment. Tantalum wire was used as filament material, and was cut to 40 cm length, then wound on a 3/16 inch rod. The filament was then stretched to a 7 cm installed length when used for HWCVD or HWECR processing.
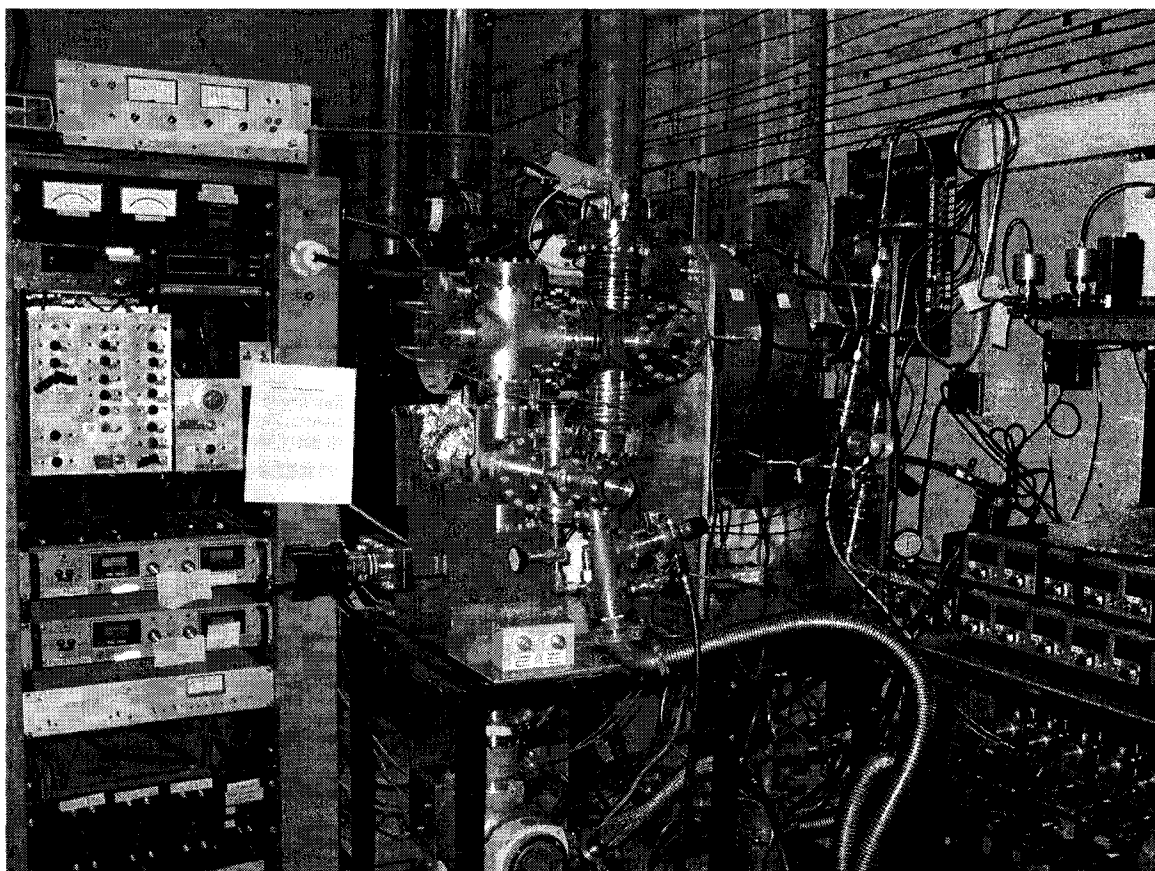

Figure A1.1: Hot-wire-ECR reactor photograph. The control rack holds an MKS baratron pressure readout, a digital ion-gauge readout, a gas flow control panel, a master gas switch, and two magnet power supplies. Mass-flow controllers are to the right in the photograph.